USArray imaging of continental crust in the conterminous United States

Xiaofei Ma and Anthony R. Lowry

Department of Geology, Utah State University, Logan, Utah 84322-4505, USA.

Key points:
- Crustal thickness and bulk crustal seismic velocity ratios are imaged by joint inversion of USArray receiver functions and gravity
- Bulk crustal composition is the larger contributor to Bouguer gravity anomaly variations
- Seismic velocity ratios are sensitive to hydration state, and Cordilleran high heat flow may partly reflect crustal hydration enthalpy

Abstract

The thickness and bulk composition of continental crust provide important constraints on the evolution and dynamics of continents. Crustal mineralogy and thickness both may influence gravity anomalies, topographic elevation and lithospheric strength, but prior to the inception of EarthScope's USArray, seismic measurements of crustal thickness and properties useful for inferring lithology are sparse. Here we improve upon a previously-published methodology for joint inversion of Bouguer gravity anomalies and seismic receiver functions by using parameter-space stacking of cross-correlations of modeled synthetic and observed receiver functions instead of standard H-κ amplitude stacking. The new method is applied to estimation of thickness and bulk seismic velocity ratio, v_P/v_S, of continental crust in the conterminous United States using USArray and other broadband network data. Crustal thickness variations are reasonably consistent with those found in other studies and show interesting relationships to the history of North American continental formation. Seismic velocity ratios derived in this study are more robust than in other analyses, and hint at large-scale variations in composition of continental crust. To interpret the results, we model the pressure/temperature-dependent thermodynamics of mineral formation for various crustal chemistries, with and without volatile constituents. Our results suggest that hydration lowers bulk crustal v_P/v_S and density, and releases heat in the shallow crust but absorbs heat in the lowermost crust (where plagioclase breaks down to pyroxene and garnet, resulting in higher seismic velocity). Hence, v_P/v_S variations may provide a useful proxy for hydration state in the crust.

1. Introduction

The formation and evolution of Earth's continental crust has broad implications for tectonism, dynamics and mass transfer processes. Open questions regarding the tectonic, melt and volatile flux processes that form the crust remain among the outstanding challenges for research in the solid Earth sciences [*DePaolo et al*.,

2008; *Williams et al.*, 2010]. Continental lithosphere is more resistant to subduction than oceanic lithosphere because of the greater buoyancy (due to greater thickness and lower density) of continental crust, resulting in a much longer and richer record of Earth history in continental lithosphere than is found in the oceans.

Seismic investigations are an important tool for assessing continental crustal composition and related evolution and dynamics [*Miller and Christensen*, 1994; *Sobolev and Bakeyko*, 1994; *Christensen and Mooney*, 1995; *Kern et al.*, 1996; *Musacchio et al.*, 1997; *Hacker et al.*, 2015], along with sampling of exposed rocks [*Rudnick and Fountain*, 1995; *Hacker et al.*, 2015] and xenoliths carried from the middle and lower crust [*Weber*, 2002; *Mengel*, 1991]. The bulk composition of the crust is andesitic with average wt-% SiO_2 generally decreasing with depth [*Rudnick and Fountain*, 1995], reflecting the repeated melt fractionation and transport processes that form typical continental crust [e.g., *Solano et al.*, 2012]. Seismic velocity and density of crustal mineral assemblages are sensitive to the bulk chemistry but also reflect the metamorphic grade at time of formation (i.e., pressure and temperature thermodynamic state) and volatile state [e.g., *Guerri et al.*, 2015; *Jones et al.*, 2015].

The EarthScope Major Research Facilities and Equipment project, funded in 2002 with instrumentation first installed beginning in 2004, was designed to identify links between surface geology and deep-Earth processes. EarthScope's USArray seismic network, including 400 three-component broadband seismographs deployed in the Transportable Array (TA) rolling network covering the entire continental United States, serves as a principal data source for this project. The TA has now completed data collection in the lower 48 United States and is currently deployed in Alaska. Our imaging of the crust uses seismic receiver functions from USArray (including the TA) as well as FlexArray and other contributed seismic networks that have been analyzed for the EarthScope Automated Receiver Survey (EARS) [*Crotwell and Owens*, 2005; *IRIS DMC*, 2010].

Several studies have used EarthScope data to image thickness and velocity properties of continental crust within the USArray footprint, with most using receiver functions [e.g., *Levander and Miller*, 2012; *Schulte-Pelkum and Mahan*, 2014], ambient noise surface wave tomography [e.g., *Porter et al.*, 2016, *Lin et al.*, 2012], regional first arrivals [*Buehler and Shearer*, 2014] or some combination of these [e.g., *Schmandt et al.*, 2015; *Shen and Ritzwoller*, 2016; *Afonso et al.*, 2016]. Our approach differs slightly from these in that we perform joint inversion of receiver functions and gravity, coupled with a thermal structure derived from Pn tomography [*Schutt et al.*, 2017], to more robustly constrain density variations and seismic velocity ratios v_P/v_S in the crust. Lowry and Pérez-Gussinyé [2011], using a similar approach, previously interpreted variations imaged in bulk crustal v_P/v_S to primarily reflect variations in abundance of quartz based on petrophysical measurements compiled by Christensen [1996] (Figure 1). Further noting a strong correlation of low v_P/v_S to high surface heat flow and high Cordilleran elevations, they hypothesized a dynamical feedback that began with localization of crustal deformation where crust had low ductile strength owing to the presence of quartz, and that lithospheric

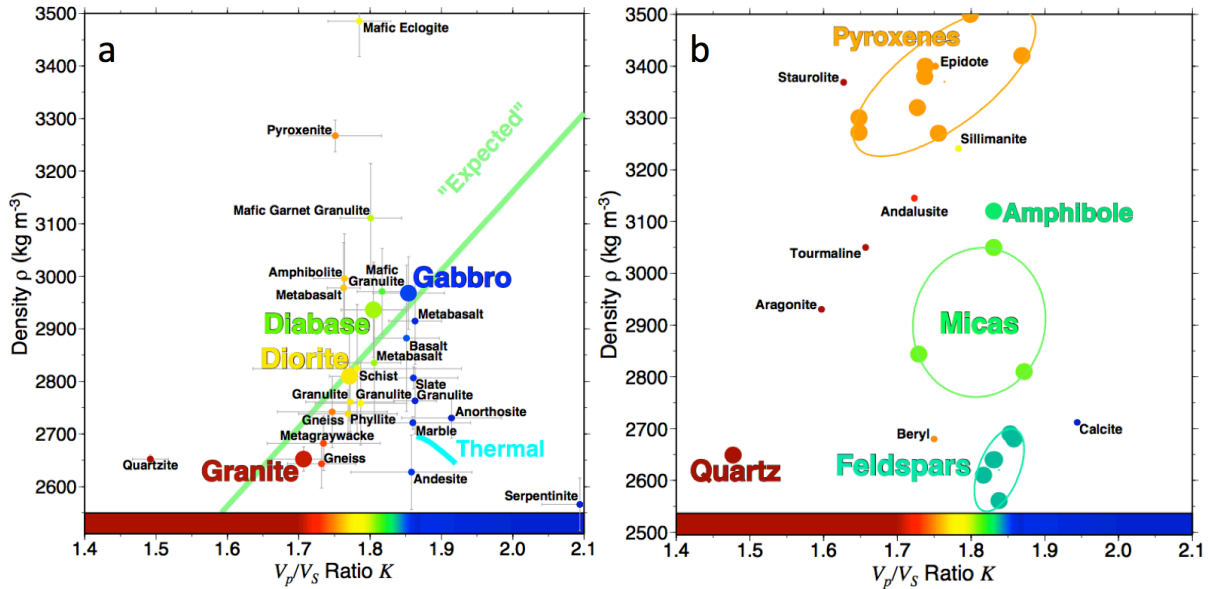viscosity was lowered further by advective warming and hydration resulting from the strain.

Figure 1. The relationship of v_P/v_S and density to mineral composition [after *Lowry and Pérez-Gussinyé*, 2011]. (a) Rock density versus v_P/v_S for various rock types using data from Christensen [1996]; the temperature dependence of v_P/v_S in anorthite for a 900°C range (cyan curve, after *Kono et al.* [2008]) is comparatively small. The green line shows the 1600 kg m^{-3} expected value of $\partial\rho/\partial\kappa$ from regression. (b) Geophysical properties for minerals (from Voigt-Reuss-Hill averages of anisotropy in Christensen [1996]) demonstrates that v_P/v_S variation in rocks is dominated by quartz content.

Water plays an important role in crustal formation by lowering the melting temperature of mantle rocks, and so seems to be a key ingredient in the seeding of thicker crust in ocean island arcs as well as the formation of more silica-rich continental crust. Water is also an important determinant for ductile rheological strength [*Kohlstedt*, 2006] and hence the mobility/stability of continental lithosphere. However, the distributions and history of hydration state in continental crust and lithosphere are generally enigmatic because of ambiguities in separating effects of chemistry, temperature, hydration and melt in remote sensing by seismic and electrical imaging, coupled with the extremely sparse in-situ sampling by xenoliths [e.g., *Jones et al.*, 2015]. In this paper, we extend an improved inversion based on the approach of Lowry and Pérez-Gussinyé [2011] to imaging of the entire conterminous United States, and we expand upon earlier interpretations of the significance of bulk crustal v_P/v_S for crustal chemistry and crustal properties by modeling the pressure-, temperature-, chemistry- and hydration state-dependence of seismic velocities and density in the crust.
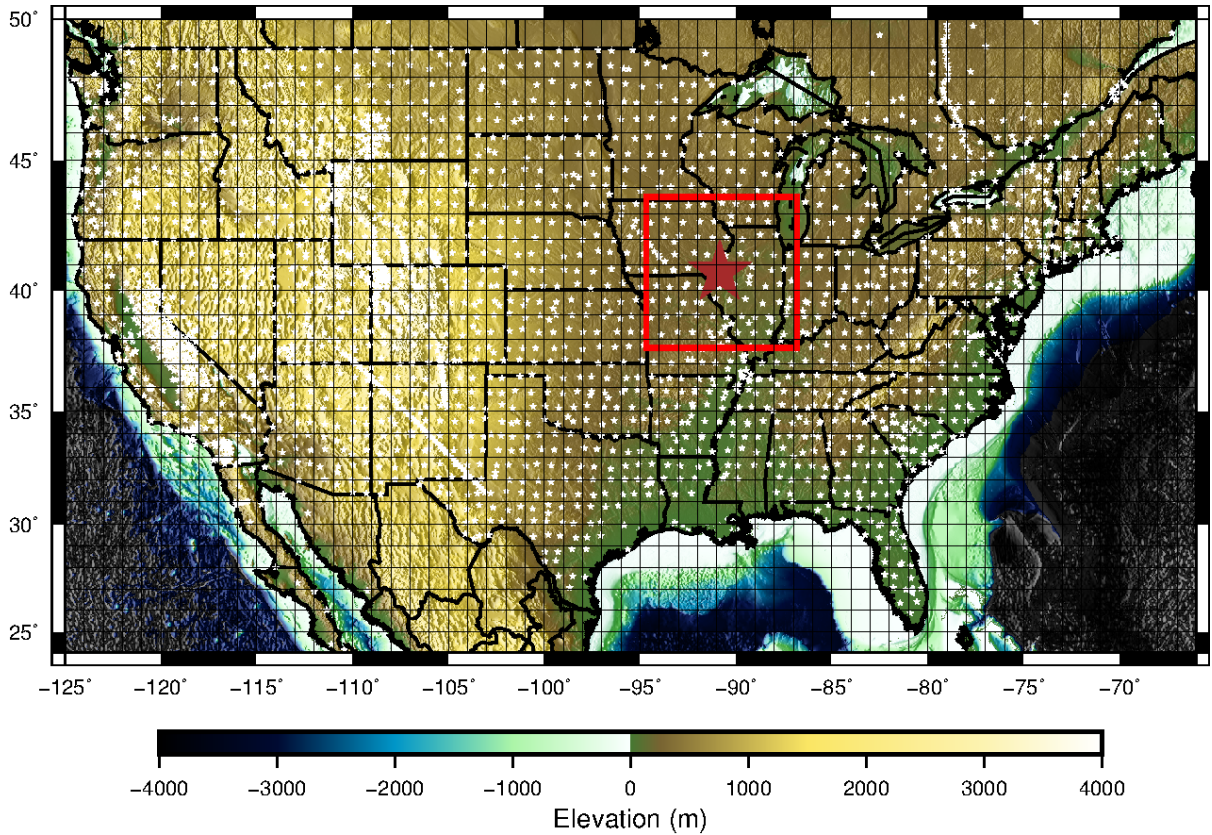
Figure 2. USArray and other seismic stations used in this analysis (stars) on a map of topographic elevation with shaded relief. All seismic stations in the EARS receiver function database [*Crotwell and Owens*, 2005; *IRIS DMC*, 2010; *Trabant et al.*, 2012] were included in the analysis, including regional networks and some PASSCAL and FLEXArray deployments. Red star is the location of seismic station TA.N41A used as an example in subsequent figures. Stochastic inversion for density parameters uses gravity and seismic fields from the entire United States; subgrids used to estimate gravity likelihoods are exemplified by the red box centered around the star at TA.N41A.

2. Methods

This paper extends an earlier analysis by Lowry & Pérez-Gussinyé [2011] that covered only the western U.S. data available at that time. The joint inversion of seismic receiver functions, gravity and spatial statistics used here to image the USArray footprint (including the conterminous United States and southernmost Canada) is similar to the methodology described by Lowry & Pérez-Gussinyé [2011]. The primary differences are the addition of newer USArray and other seismic data (Figure 2), and three modifications to the joint inversion methodology designed to improve performance. First, instead of using EARS parameter-space stacks of receiver function amplitudes [*Zhu and Kanamori*, 2000; *Crotwell and Owens*, 2005], we built a library of synthetic receiver functions and stacked cross-correlation coefficients relating synthetic to observed receiver functions from the EARS database [*IRIS DMC*, 2010] in the crustal thickness and v_P/v_S parameter space. Second, we implemented a stochastic inversion for density parameters associated

with crustal thickness, v_P/v_S and thermal contributions to gravity. Finally, we estimated and removed gravity anomalies due to geothermal variations in the lithosphere using a combination of surface heat flow and Moho temperature estimates derived from Pn tomography [*Schutt et al.*, 2016; 2017] instead of surface heat flow alone.

2.1. Data

Data for this analysis are from the EarthScope Automated Receiver Survey (EARS) [*Crotwell and Owens*, 2005; *IRIS DMC*, 2010; *Trabant et al.*, 2012], with station locations shown in Figure 2. We used EARS receiver functions only for those seismic events with a radial match for the iterative deconvolution [*Ligorría and Ammon*, 1999] exceeding 80%.

2.2 Receiver Function Synthetics and Cross-Correlation Stacking

EARS [*Crotwell and Owens*, 2005] H-κ amplitude stacks were used in the analysis of Lowry and Pérez-Gussinyé [2011], but here we introduce a new approach to parameter-space receiver function analysis. Typical H-κ stacking approaches to estimating bulk crustal properties [e.g., *Zhu and Kanamori*, 2000] stack the amplitudes at arrival times predicted for the Ps Moho conversion, the PpPs reverberation, and the PpSs+PsPs reverberation given a range of assumed crustal thickness and v_P/v_S. Each of these phase arrivals is weighted equally for each event in the amplitude stack, but in practice the relative scaling of the receiver function arrival amplitudes depends on the Moho impedance contrast, the ray parameter of the event, and interference from phases deriving from other impedance contrasts. Hence, we instead compare (via cross-correlation) the full waveform of each receiver function to synthetic receiver functions generated using a synthetic receiver function code [*Ammon*, 1991].

A library of synthetic receiver function models was calculated, parameterized by crustal thicknesses ranging from 20 to 60 with sample mesh 0.25 km, and v_P/v_S from 1.6 to 2.1 at a 0.025 mesh, for a total of 3200 models. Each synthetic model assumes a uniform isotropic crustal layer with P velocity 6.3 km/s. Bulk crustal v_P is not uniform across the U.S., instead ranging from 6.1 to 6.5 km/s based on crustal-scale seismic reflection and refraction data [*Smith* et al., 1989; *Pakiser*, 1989; *Braile et al.*, 1989]. Building a larger library would be computationally expensive, and Zhu and Kanamori [2000] note that a 0.1 km/s error in crustal v_P translates to a timing error equivalent to only a 0.5 km error in crustal thickness. Uppermost mantle velocity varies from 7.7 to 8.4 km/s [*Buehler and Shearer*, 2017], but mantle velocity impacts only amplitude of phases and does not affect arrival time. The cross-correlation method described here is relatively insensitive to amplitude, so our synthetics assume a constant 8.0 km/s upper mantle.

The synthetic receiver function modeling approach of Ammon [1991] specifies a white-noise level, C, to prevent numerical singularity of the deconvolution. We tested values for C ranging from 0.1 to 0.0001 and settled on 0.0001 as the most robust. The algorithm also specifies a Gaussian filter width, a. We adopt $a = 2.5$ s as used

by EARS to generate the observed receiver functions. All observed receiver
functions were resampled to 10 Hz, the sample rate of the synthetic receiver function.
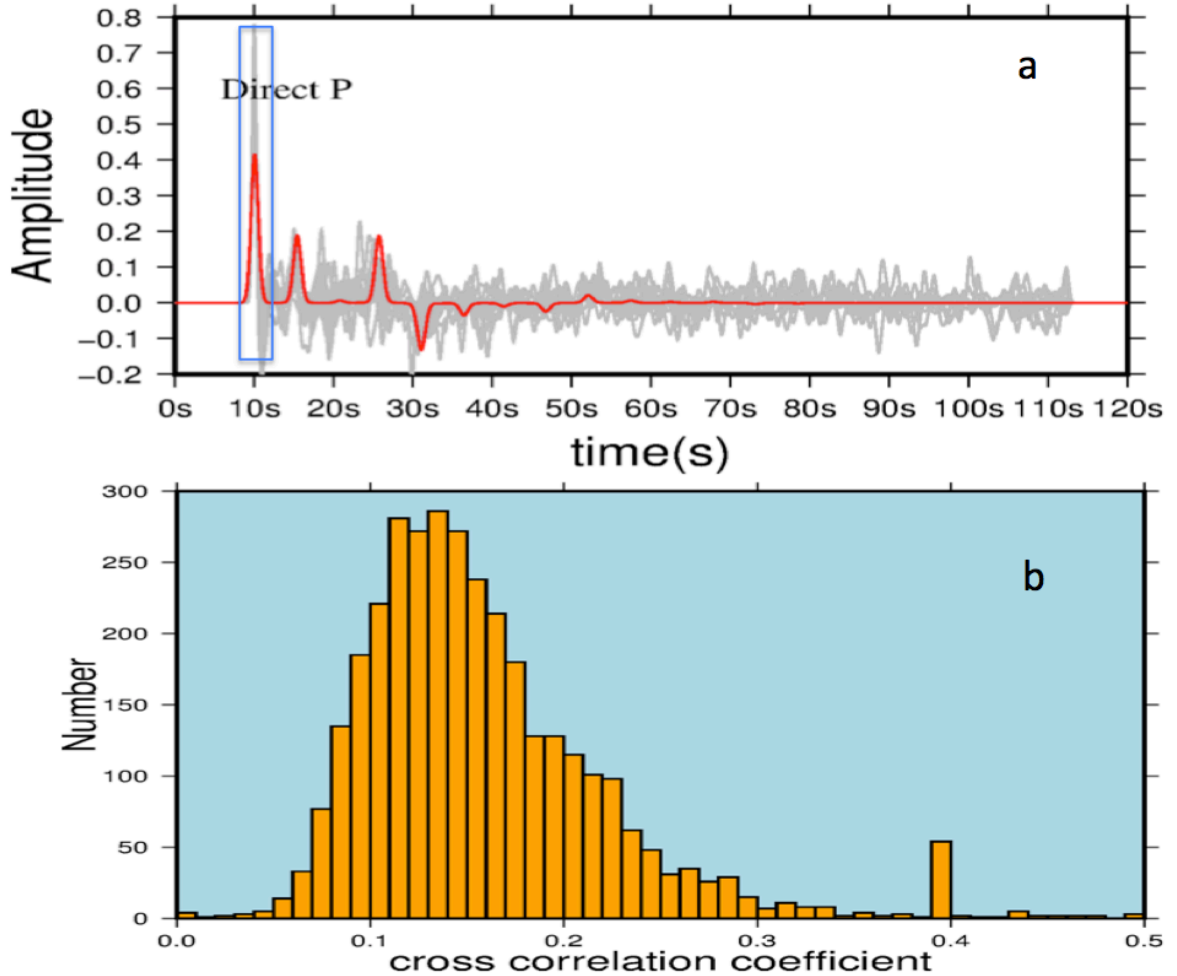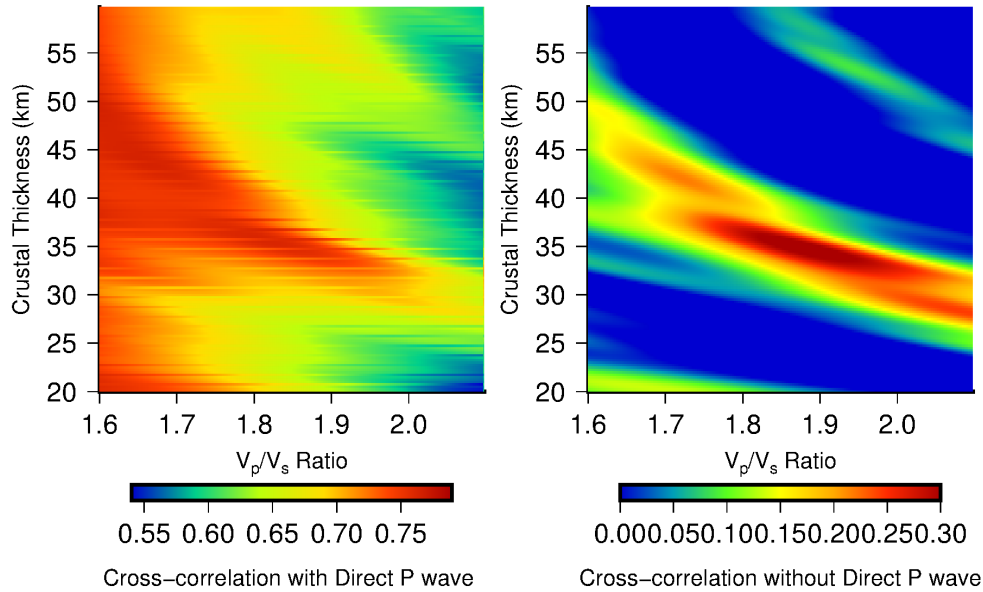

Figure 3. Example observed and modeled synthetic receiver functions. (a) Observed EARS
radial receiver functions (grey) for 54 events at site TA.N41A, and the synthetic receiver
function that correlated most strongly with the observed receiver functions (red). The direct
P arrival inside the blue rectangle is not included in cross-correlation calculations. (b)
Histogram of the maximum averaged cross-correlation coefficients found at each of the
>3000 sites in the study region; the median maximum cross-correlation is 0.14.

Before cross-correlating, the observed and synthetic receiver functions were aligned
to impose coincident timing of the direct P arrival, after which the direct P arrival in
each was masked so that only the later phase arrivals were included in the cross-
correlation calculation (Figure 3). This is done because the only useful information
content in the P arrival, for our purposes, is the reference time of the receiver
function, and including the P phase degrades the resolving power of the receiver
function correlations (as shown in Supplemental Material Figure S1). We average
the cross-correlations for all earthquake events as a function of the crustal thickness

(H) and seismic velocity ratio v_P/v_S assumed in the synthetic model, analogous to the H-κ parameter-space representation used in amplitude stacking [*Zhu and Kanamori*, 2000]. Like with H-κ stacking, the raw cross-correlation stacks exhibit several local maxima (Figure 4a). The largest cross-correlation coefficients tend to be low, with median maxima around 0.14 (Figure 3). For example, the maximum cross-correlation coefficient at station TA.N41A is 0.19 at H = 35 km and v_P/v_S = 1.93 (Figure 4). A secondary local maximum occurs at H = 45 km, v_P/v_S = 1.7, and a tertiary maximum occurs at a crustal thickness of 20 km and v_P/v_S of 1.72.

Supplemental Figure S1. Example cross-correlations for TA.N41A with the direct P phase included (left) and with the P phase masked (right). Correlation coefficients are much higher with the P phase included but the resolving power for determining crustal structure parameterization is greatly reduced.

Averaged cross-correlations are low with multiple maxima in part because the real-Earth crust is not a single uniform layer as our modeling assumes. Converted phases are generated at all impedance contrasts in the crust and mantle, and both crustal thickness and v_P/v_S can vary on scales sampled by the conversions and reverberations from different azimuths of earthquake events at a single site. Cross-correlations are significantly reduced by differences in the receiver functions for different events with different back-azimuths. For example, we took the receiver function from the largest event recorded at station TA.N41A (a M8.4 event, with the second-highest radial match of 98.2%) and compared to all other events using our cross-correlation approach. The resulting average cross-correlation was 0.32. This relatively low correlation of events is likely some combination of "noise" in the receiver function estimate (loosely characterized in the EARS receiver functions by radial match of the deconvolution, in which events with match <80% are rejected [*Crotwell and Owens*, 2005]) and back-azimuth-dependent variations in timing and amplitude related to layer heterogeneity and anisotropy effects [e.g., *Schulte-Pelkum*

and Mahan, 2014]. The additional difference between a cross-correlation of 0.32, representing the maximum theoretically possible for a 1D, isotropic Earth model at station TA.N41A, and the 0.19 maximum of our comparison to synthetic models likely relates to some combination of multiple layering of the real-Earth lithosphere, and differences in layer impedance from that assumed by the synthetic. Regardless, the cross-correlation approach introduced here produces secondary maxima that are generally much smaller relative to the global maximum than standard H-κ stacking like that used in the joint inversion of Lowry and Pérez-Gussinyé [2011] (Figure 4b).
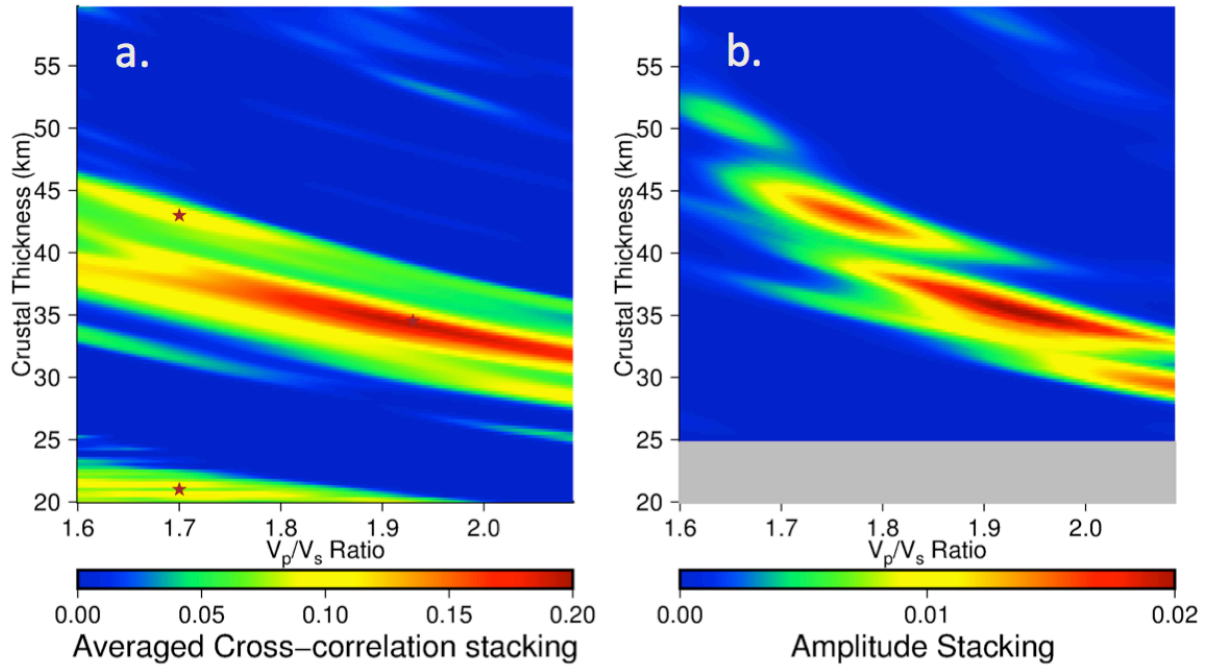

Figure 4. Example parameter-space receiver function analyses at seismic station TA.N41A. (a) Cross-correlations of observed and modeled receiver functions, averaged for 54 earthquake events, as a function of crustal thickness H and v_P/v_S assumed in the synthetic model. Local maxima are marked by stars. The global maximum averaged cross-correlation is 0.19 at H = 35 km, v_P/v_S = 1.93. The local maximum at H = 20 km likely reflects P-to-S conversions at the mid-crustal interface. (b) EARS [*Crotwell and Owens*, 2005] amplitude stack. Similar to the H-κ amplitude stacking approach [*Zhu and Kanamori*, 2000], cross-correlation maxima in (a) are elongate along the v_P/v_S axis so are more sensitive to crustal thickness than v_P/v_S, but secondary maxima of the cross-correlation averages are diminished relative to those of amplitude stacks and hence less likely to be mistaken for the true model.

2.3 Gravity Modeling

The receiver functions observed at a single seismic station are not the only pieces of information that constrain this problem, as both gravity and the spatial statistics of estimates at neighboring sites afford additional predictive power. Individual contributions to the total Bouguer gravity anomaly field from crustal thickness H, bulk

v_P/v_S κ and thermal variations T are scaled by density parameters $\Delta\rho_{\text{Moho}}$ for the density contrast at the Moho, $\partial\rho/\partial\kappa$ for the change in density for given change in v_P/v_S, and a coefficient of thermal expansion α_v, respectively. Gravity due to crustal thickness variations is modeled as [*Lowry and Pérez-Gussinyé*, 2011]:

$$\tilde{B}_H = 2\pi G \Delta\rho_{\text{Moho}} \tilde{H} \exp(-k\bar{H}) \tag{1}$$

in which the overbar indicates the mean of a field, the tilde ~ denotes 2D Fourier-transformed amplitudes of a field with the mean removed (e.g., $\tilde{H} = F\{H(x,y) - \bar{H}\}$ where $F\{\bullet\}$ denotes the 2D Fourier transform operator); G is the universal gravitational constant; and k is the modulus of 2D wavenumber associated with each amplitude. Variations in bulk v_P/v_S are assumed to be uniformly distributed with depth and the associated gravity anomalies are calculated as:

$$\tilde{B}_\kappa = 2\pi G \frac{\partial\rho}{\partial\kappa}\left[\frac{1 - \exp(-k\bar{H})}{k}\tilde{K} - \tilde{M}\exp(-k\bar{H})\right] \tag{2}$$

Here, $\tilde{M} = F\{(H - \bar{H})(K - \bar{K})\}$ is a correction factor for mass associated with varying crustal thickness and v_P/v_S at the Moho. Finally, gravity anomalies associated with thermal variations are calculated from the three-dimensional temperature field model described in section 2.7 via:

$$\tilde{B}_T = \int_0^{200} 2\pi G \alpha_v \bar{\rho}(z)\tilde{T}(z)\exp(-kz)dz \tag{3}$$

We derive $\bar{\rho}(z)$ from mean temperatures in the geothermal model combined with expected density for a mean continental crustal composition [*Christensen and Mooney*, 1995]. Gravity associated with the thermal boundary layer model is integrated only to a depth of 200 km, beyond which the assumptions of steady-state conduction and constant mantle potential temperature in the thermal modeling (described in a subsequent section) may no longer be representative of actual temperature variation.

2.4 Stochastic Inversion for Density Parameters

In practice, we do not know the density parameters $\Delta\rho_{\text{Moho}}$, $\partial\rho/\partial\kappa$ and α_v a priori. The green line in Figure 1a, derived from a weighted regression of the measurements in Christensen [1996], implies $\partial\rho/\partial\kappa$ = 1600 kg/m^3, but scatter in the relationship is obviously large. The globally averaged Moho density contrast $\Delta\rho_{\text{Moho}}$ estimated for the Preliminary Preferred Earth Model (PREM) [*Dziewonski and Anderson*, 1981] is 480 kg/m^3, and Tenzer et al. [2012] estimated a similar 485 kg/m^3 from independent seismic and gravity observations. However, Martinec [1994] estimated a 280 kg/m^3 Moho contrast under the continents, and regional variations in Pn velocity [e.g., *Buehler and Shearer*, 2017], coupled with a large possible range of lower crustal

densities for mafic to felsic compositions, implies density contrasts ranging from 160 kg/m^3 to 440 kg/m^3 [*Niu and James*, 2002; *Julià*, 2007].

Instead of assuming density parameters a priori, we estimate them from the relationship of the model predictions to observed Bouguer gravity over the entire Transportable array footprint using a stochastic inversion approach. Lowry and Pérez-Gussinyé [2011] inverted for density parameters from the model fields using an ordinary least-squares approach, but this produces density parameters that are much lower than those expected based on laboratory and geophysical constraints because the model fields are cross-correlated, yielding an ill-conditioned matrix. Stochastic inversion stabilizes ill-conditioned problems analogously to damped least-squares, but using probabilistic information rather than ad-hoc damping. Stochastic inversion assumes a known expected value, $\langle \vec{m} \rangle$, for the model parameter vector, $\vec{m}$, and a known parameter covariance matrix, $\overline{\overline{C}}_m$, for the model parameters. We then solve for differences of the true model parameters from the expected values,

$$\Delta \vec{m} = \vec{m} - \langle \vec{m} \rangle \ , \quad \text{as} \quad \Delta \vec{m} = \left(\overline{\overline{G}}^T \overline{\overline{G}} + \overline{\overline{C}}_m^{-1} \right)^{-1} \overline{\overline{G}}^T \Delta \vec{d} \ , \quad \text{in which} \quad \overline{\overline{G}} = \left[\begin{array}{ccc} \vec{B}_H^1 & \vec{B}_\kappa^1 & \vec{B}_T^1 \end{array} \right] \quad \text{using}$$

amplitudes in equations (1)–(3) with density parameters set to one; and $\Delta \vec{d} = \vec{B}_{obs} - \overline{\overline{G}} \langle \vec{m} \rangle$ for observed Bouguer gravity amplitudes $\vec{B}_{obs}$.

Our analysis uses observed Bouguer gravity anomalies from WGM2012 [*Balmino et al.*, 2011; *Bonvalot et al.*, 2012]. We assign expected values and standard deviations for the density parameters as $\langle \Delta\rho_{\text{Moho}} \rangle$ = 300 ± 60 kg/m^3 [*Ito and Simons*, 2011]; $\langle \partial\rho/\partial\kappa \rangle$ = 1600 ± 300 kg/m^3 based on the regression of Christensen et al. [1996] measurements in Lowry and Pérez-Gussinyé [2011]; and $\langle \alpha_v \rangle$ = 3.5×10^{-5} ± 3×10^{-6} after Afonso et al. [2005]. Some of these density parameters can be expected to covary as well: notably, the Moho density contrast $\Delta\rho_{\text{Moho}}$ is partly a function of the density of the overlying crust, which we parameterize as the density derivative with respect to v_P/v_S, $\partial\rho/\partial\kappa$. However, a portion of that covariance is independently modeled by the $\tilde{M}$ correction factor in equation (2), so $\Delta\rho_{\text{Moho}}$ can be conceptualized as a reference value that should approximate the mean density contrast of the region being modeled. We assume zero off-diagonal parameter covariances, as we lack laboratory or geophysical measurements suitable to constrain independently the covariance of (for example) the continental-scale reference value of $\Delta\rho_{\text{Moho}}$ with $\partial\rho/\partial\kappa$. The density parameters are estimated for large-scale grids covering all of the study area (Figure 2) and are recalculated with each new update to the seismic models of crustal thickness and v_P/v_S used in the calculation of gravity models $\vec{B}_H^1$ and $\vec{B}_\kappa^1$, respectively. In later sections we also will examine density parameters independently calculated for the eastern and western halves of the conterminous U.S.

2.5 Spatial Statistics and Optimal Interpolation

To generate gridded values of crustal thickness H and seismic velocity ratio κ needed for the gravity modeling, we must interpolate estimates of the seismic properties at irregularly-spaced seismic sites to a constant-spaced grid. For this we use optimal interpolation (OI), also called "kriging", an interpolation method that relies on the spatial statistics of measured data to estimate the most likely value and uncertainty at an unsampled location [*Davis*, 1986]. Optimal interpolation uses the variogram statistics of a field, an expression of the expected value of the difference between measurements as a function of the distance between the measurements.

Variograms of crustal thickness H and v_P/v_S are estimated directly from the estimates at pairs of individual seismic stations by binning according to the distance between the stations (Figure 5). Ideally, the variogram at zero distance reflects the variance of individual measurements while the variogram at large distances represents the global variance of the field. A spherical parametric model of the variogram estimates is used to invert for optimal weights applied to the estimates at sites surrounding an interpolation location, and the weights plus a Lagrange variable provide an estimate of the variance of the interpolation estimate. In addition to affording gridded interpolations of the seismic fields, optimal interpolation expected values and variance will be used to generate OI-likelihood functions at a seismic station location based on the estimates at nearby sites.
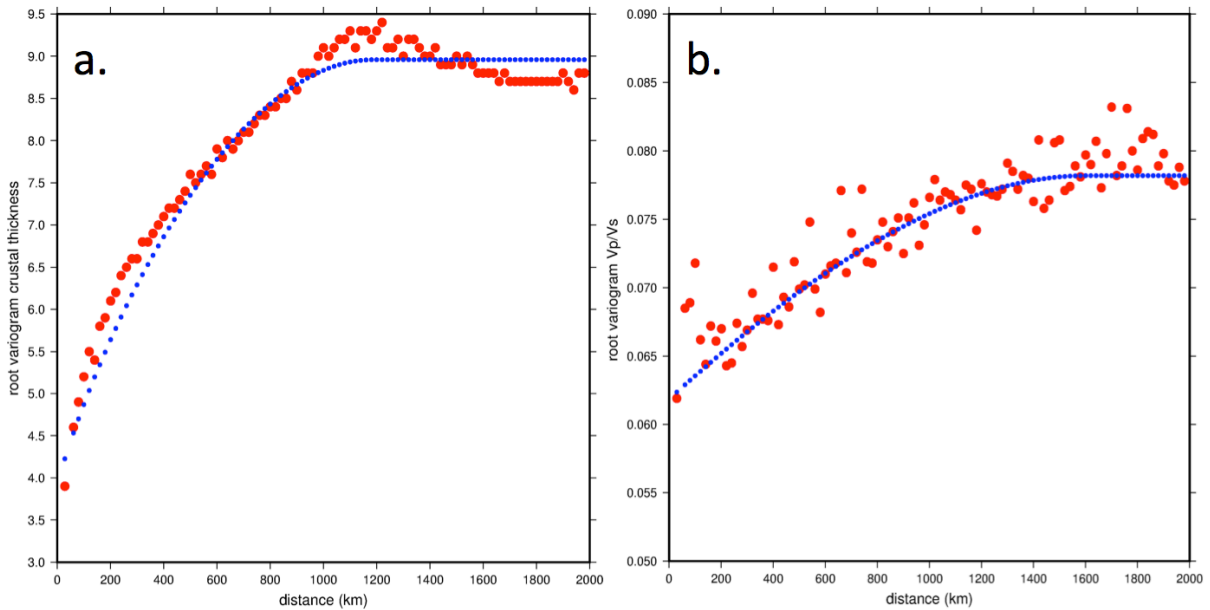

Figure 5. Root-variograms of (a) crustal thickness and (b) v_P/v_S corresponding to the root-mean square difference between measurements as a function of distance. Red circles are derived from all of the raw measurements after binning by distance between measurements; blue circles depict a spherical parametric model (approximating the observed distribution) that was used for optimal interpolation.

2.6 Joint Inversion with Gravity and OI Likelihood Filters

The joint inversion for crustal thickness and bulk crustal v_P/v_S is applied iteratively over all of the seismic stations in the study area (Figure 2). First, a gravity likelihood filter is calculated using a 640×640 km window centered at the station slated for update, S_i. The crustal thickness H and v_P/v_S κ for station S_i are treated as unknown variables, while prior estimates of H and κ at surrounding stations are temporarily held fixed. For each possible combination of $(H, \kappa)_j$ in the parameter space at station S_i, we interpolate (H, κ) at S_i and the surrounding sites to a 20 km-spaced grid. The grids are used to model the gravity via equations (1)-(3) using density parameters derived from stochastic inversion of the larger grid as described in section 2.4. The L_2-norm, R, of the difference between observed and modeled gravity is calculated for each assumed $(H, \kappa)_j$, and contours of the misfit are used to calculate associated confidence intervals $(1 - \alpha)$ via the likelihood ratio method [*Beck and Arnold*, 1977]:

$$R^2 \le R_{\min}^2 \left(1 + \frac{M}{N_g - M} F_\alpha^{-1}\left(M, N_g - M\right) \right) \tag{4}$$

Here, $R_{\min}$ is the global minimum gravity L_2 norm, M is the number of model parameters (i.e, two corresponding to H and κ at the seismic site S_i), N_g is the number of gravity observations, F^{-1} is the inverse of the F-cumulative distribution function and α is probability. The likelihood of the model given the data corresponds to the probability density function described by $(1 - \alpha)$, after normalization to yield an integral over the parameter space equal to one. An example gravity likelihood function for station TA.N41A (without normalization) is given in Figure 6b.

Optimal interpolation provides estimates of both the expected values $\left(\langle H \rangle, \langle \kappa \rangle\right)$ and standard deviations $\left(\sigma_H, \sigma_\kappa\right)$ of interpolated fields. To create the OI-likelihood filter, we interpolate estimates of crustal thickness and v_P/v_S at the nearest 150 seismic sites to the location of seismic station S_i. The C_{OI} confidence interval of any arbitrary $(H, \kappa)_j$ in the 2D parameter space (where C_{OI} represents a real-valued multiple of normalized σ) can be calculated via:

$$C_{OI}^2\left((H, \kappa)_j\right) = \left(\frac{H_j - \langle H \rangle}{\sigma_H}\right)^2 + \left(\frac{\kappa_j - \langle \kappa \rangle}{\sigma_\kappa}\right)^2$$

which has corresponding probability density function:

$$\alpha = \frac{1}{2\pi} \exp\left(-\frac{C_{OI}^2}{2}\right).$$

An example OI likelihood function (without the normalization constant) is shown in Figure 6a.

Finally, both likelihood functions are multiplied by the stacked cross-correlations between modeled and observed receiver functions. This multiplication of probability

12

density functions is thus essentially a Bayesian approach to inversion. In practice, the normalization constants are neglected, as they affect only the scaling and not the shape or maxima of the resulting product, which is why likelihoods in Figure 6 are shown with a maximum of one. The crustal thickness and v_P/v_S at station S_i are then updated to the maximum of the likelihood-filtered cross-correlation stack (Figure 6d).
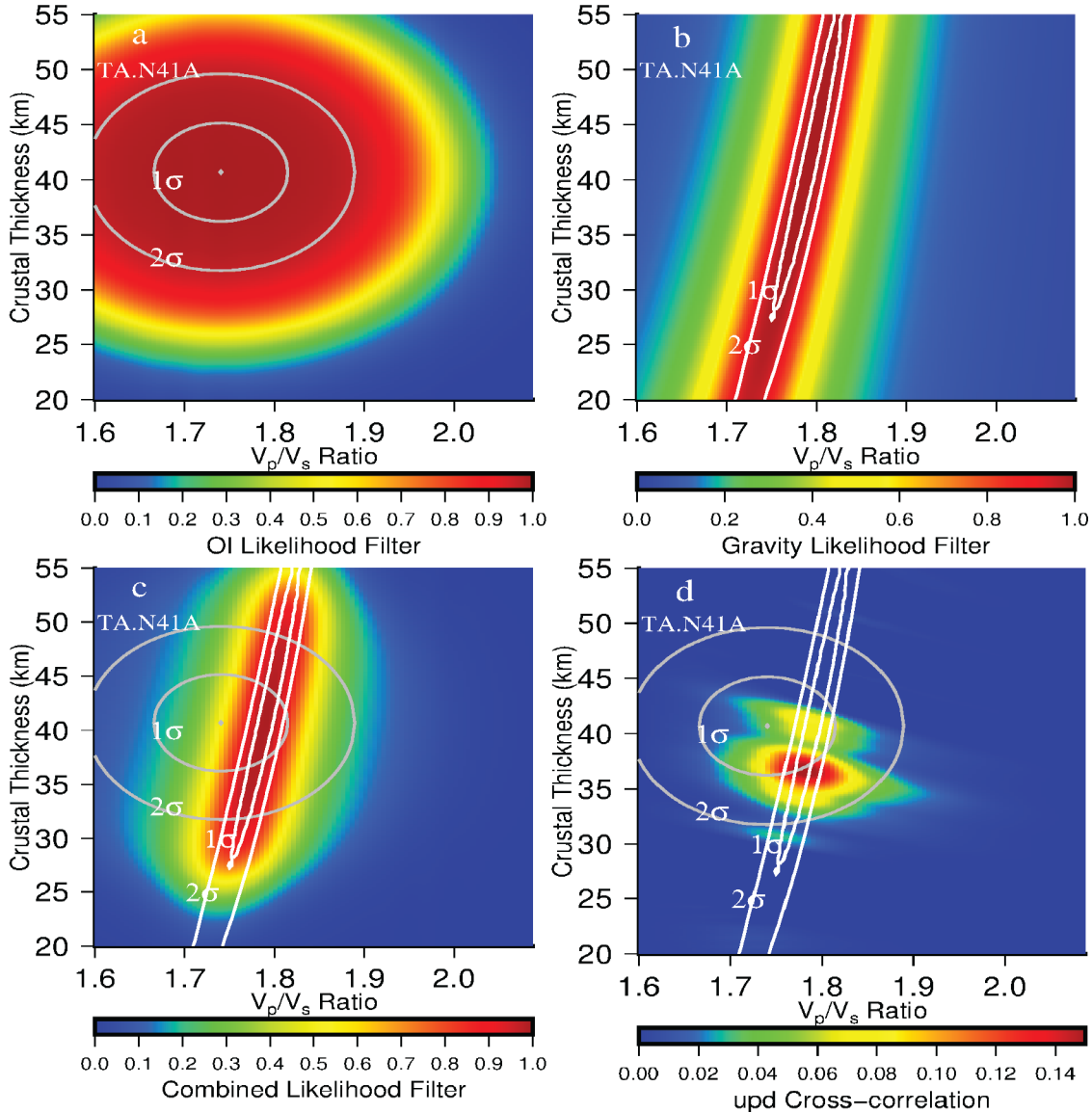

Figure 6. Example parameter-space likelihood maps for joint inversion at seismic station TA.N41A. (a) Optimal interpolation likelihood; (b) gravity likelihood; (c) the combined likelihood of OI and gravity; and (d) receiver function cross-correlation stack after likelihood filtering (compare with Figure 4, the raw cross-correlation stack at TA.N41A).

13

2.7. Thermal Model

As was done in Lowry and Pérez-Gussinyé [2011], we use a geothermal model patterned after Lowry et al. [2000] to reduce potential bias of mass estimates in the gravity modeling by anticorrelation of the thermal and crustal thickness fields (e.g., due to coupled crustal thinning and advective warming of the lithosphere by extensional strain). The earlier analysis used surface heat flow and surface heat production to estimate geotherms throughout the study region, where in our analysis we use both surface heat flow and an estimate of Moho temperature derived from Pn velocity tomography and mineral physics [*Schutt et al.*, 2016; 2017] as our observables. Measurements of spatially-varying surface heat production were not used in this model after analyses showed that aerospectral gamma radiation measurements of (shallow: <1 m) surface heat production yielded no improvement in the agreement of surface heat flow and Pn geotherm models [*Berry et al.*, 2014]. There are large discrepancies between the Moho temperatures predicted by conductive thermal modeling of surface heat flow and those measured from Pn that cannot be removed by varying thermal parameters describing thermal conductivity or radioactive heat production [*Berry et al.*, 2015], so for this analysis we calculate two 1D geotherms at each map location. One geotherm, $T_q(z)$, parameterized a conductive thermal length-scale, l_{con}, for the diffusive error-function based on the surface heat flow; the other, $T_{Pn}(z)$, chose l_{con} to match the Pn Moho temperature, but both used otherwise identical parameters to describe temperature-dependent thermal conductivity, depth-dependent distribution of radioactive heat production, and mantle potential temperature. The final geotherm was a crude linear combination of the two using:

$$T(z) = \left(1 - \frac{z}{H}\right) T_q(z) + \left(\frac{z}{H}\right) T_{Pn}(z)$$

in the crust and $T(z) = T_{Pn}(z)$ in the mantle. This effectively forces the final geotherm to be more similar to the shallow observations in the shallow crust, where transients, topographically-driven hydrologic flow, and other non-steady-state and advective processes are known to perturb heat flow observations [e.g., *Smith and Chapman*, 1983; *Ehlers*, 2005], and more similar to the deep temperature measured at depth. Gravity modeling of this temperature model was found to significantly reduce gravity residuals in our models relative to geotherms derived from surface heat flow alone, lending confidence that the model is indeed an improvement. We discuss a possible mechanism for the observed discrepancy between deep and shallow heat transfer observations in section 4.

3. Results

We ran the joint inversion algorithm described in section 2 for more than ten iterations over all of the >3000 seismic sites in the study region (Figure 2). The results after multiple iterations significantly reduce the spatial variance of crustal thickness and v_P/v_S parameters relative to the estimates derived from raw cross-correlation stacks, particularly in the case of v_P/v_S. Measurement standard deviations

(i.e., the zero-distance bin of variograms in Figure 5) decreased from 9.7 to 4.0 km for crustal thickness and 0.16 to 0.07 for v_P/v_S, while global standard deviations dropped from 11.8 to 8.7 km and 0.17 to 0.08 respectively. The jointly-inverted estimates of crustal thickness are shown draped over topographic relief in Figure 7, and our v_P/v_S estimates are shown in Figure 8.
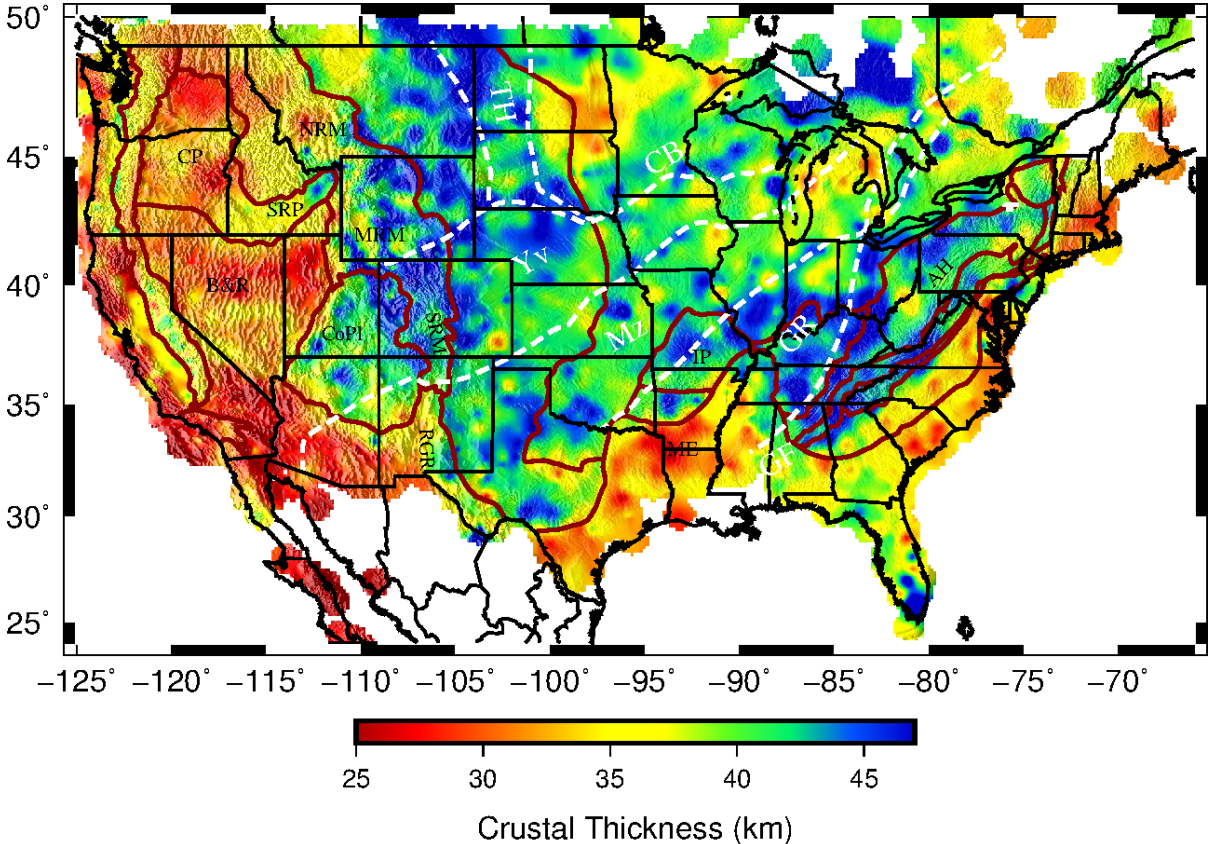

Figure 7. Map of crustal thickness, draped over shaded topographic relief. The averaged crustal thickness is 38.9 km. Physiographic province boundaries are shown in red and labeled with black text; dashed white lines with white labels are Precambrian basement features after Whitmeyer and Karlstrom [2007]. AH denotes Appalachian Highlands; B&R: Basin & Range province; CB: Cheyenne belt; CoPl: Colorado Plateau; CP: Columbia Plateau; GF: Grenville Front; GR: Granite-Rhyolite province; IP: Interior Plain; ME: Mississippi embayment; MRM: middle Rocky Mountains; Mz: Mazatzal; NRM: northern Rocky Mountains; RGR: Rio Grande rift; SRP: Snake River plain; SRM: southern Rocky Mountains; TH: Trans-Hudson orogeny; Yv: Yavapai.

Our estimates of crustal thickness (Figure 7) are qualitatively similar to results of other studies of using different methods [e.g., *Prodehl*, 1970; *Braile et al.*, 1989; *Schmandt et al.*, 2015; *Shen and Ritzwoller*, 2016]. A quantitative comparison to the model of Schmandt et al. [2015], which used common conversion point stacking of receiver functions in combination with Rayleigh wave modeling of velocity, yields a mean difference of 1.7 km with standard deviation of 4.0 km (which is roughly equal to our method's measurement uncertainty in Figure 5). The averaged regional

crustal thickness is 38.9 km. The thinnest crust in the western U.S. is associated with oceanic-derived accretionary terranes and highly extended lithosphere in rift zones. Thicknesses less than 30 km occur along the Pacific coastline, in the southern Basin & Range province, in the northernmost part of the northern Basin and Range, and along the eastern and southern edges of the Columbia Plateau (which is part of the Siletzia terrane [*Schmandt and Humphreys*, 2011]). The crust under the Cascade and Sierra-Nevada mountain ranges and the Snake River plain is slightly thicker, ~35–40 km. The Great Plains, middle and southern Rocky Mountains, Colorado Plateau and Wyoming have the thickest (~45–55 km) crust in the western U.S. One minor difference between our model and other USArray models [*Schmandt et al.*, 2015; *Shen and Ritzwoller*, 2016] is that our inversion finds a ~5-km thinner crust along the southern boundary of the northern Rocky Mountains, isolating the thicker, magmatically-inflated Snake River plain crust to the south [*McCurry and Rodgers*, 2008] from moderately extended crust in the northern Rocky Mountains. In the eastern U.S., the thinnest crust (<30 km) is found in the Coastal Plains of the Mississippi Embayment and where attenuated by Atlantic rifting along the Atlantic coastline, although there is also surprisingly thin crust (~35 km) straddling the Great Plains/Central Lowlands boundary in the southwestern Superior province. The crust under the Great Lakes, Illinois Basin and southern Canada has mostly intermediate thickness of 37–42 km. The Appalachian Highlands by contrast have crustal thickness up to 50+ km. Of the Precambrian basement provinces, the Yavapai and Granite-Rhyolite provinces have generally thicker crust than the Mazatzal province.

Estimates of western U.S. crustal v_P/v_S have been published previously in Lowry and Pérez-Gussinyé [2011] using a precursor to this inversion method, Buehler and Shearer [2014] using station terms from Pn/Sn tomography, and Steck et al. [2011] from Pg/Sg tomography. The pattern of variations in Figure 8 is (unsurprisingly) broadly similar to those of Lowry and Pérez-Gussinyé [2011], but with significant differences in the scaling and some small-scale patterns. Roughly 98% of our v_P/v_S estimates fall between 1.7 and 1.9, whereas ~15% of the estimates in Lowry and Pérez-Gussinyé [2011] are over 1.9. We attribute the change to improved characterization of the density parameters by the switch to stochastic inversion described in section 2.4. v_P/v_S is poorly constrained by receiver function seismic constraints alone (see e.g. Figure 4), making the gravity constraint an important contributor to the final estimate. As a consequence however, the $\partial\rho/\partial\kappa$ density parameter plays a pivotal role in "scaling" the pattern of variation of v_P/v_S. The stochastic inversion approach yields larger density parameters that are more similar to those one would infer from laboratory measurements (Figure 1), resulting in a steeper slope for gravity confidence intervals on the (H, κ) parameter space (e.g., Figure 6b) and a tighter resulting range (and corresponding reduced variance) of v_P/v_S. Where the models overlap, the overall pattern of variation of bulk crustal v_P/v_S is very similar to that of Lowry and Pérez-Gussinyé [2011] despite the difference in variance, and they differ by only 0.04 ± 0.05 (i.e., within measurement uncertainties). However the reduced overall variance of this model is encouraging in that the vast

majority of estimates fall within the range encompassed by measurements of crustal rocks (Figure 1a). Both Buehler and Shearer [2014] and Steck et al. [2011] noted some similarities in patterns of their v_P/v_S estimates to those of Lowry and Pérez-Gussinyé [2011], but both also noted significant discrepancies, the origins and significance of which are unclear.
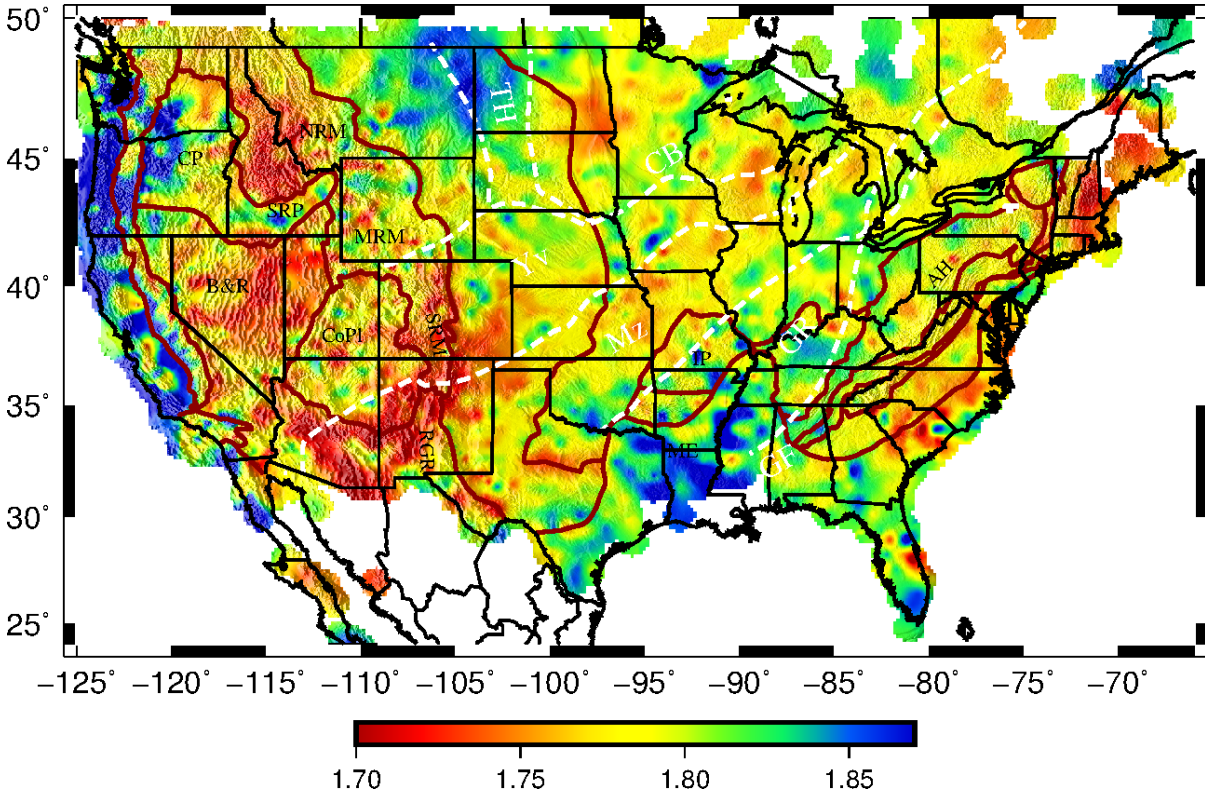

Figure 8. Map of jointly-inverted bulk crustal v_P/v_S. The averaged v_P/v_S is 1.79. Physiographic and Precambrian basement provinces are as in Figure 7.

The average v_P/v_S of the study area is 1.79. Low v_P/v_S (<1.75) is prevalent in the southern Rocky Mountains, Rio Grande rift, northern Rocky Mountains and northern Basin and Range provinces. The western half of the Colorado Plateau has an intermediate v_P/v_S ~1.8, while the eastern Colorado Plateau is nearer 1.72. The Snake River plain and oceanic-derived terranes along the Pacific coast have high v_P/v_S ~1.83-1.88. The northwestern Basin and Range, central Wyoming and northeastern Snake River plain have locally much higher v_P/v_S than surrounding regions where tomography studies find low shear velocity in the lower crust [*Wagner et al.*, 2012; *Schmandt et al.*, 2015], suggesting some high v_P/v_S may reflect lower crustal melts. v_P/v_S is generally high in the northern Great Plains, and lower in the southern and eastern Granite Rhyolite provinces except near strong gravity highs such as those of the southern Oklahoma Aulacogen and the Midcontinent rift, which have very high v_P/v_S. The Mississippi Embayment has generally high v_P/v_S and high v_P/v_S pockets are also observed in the Appalachian Highlands, while eastward from there to the Piedmont v_P/v_S is relatively low.
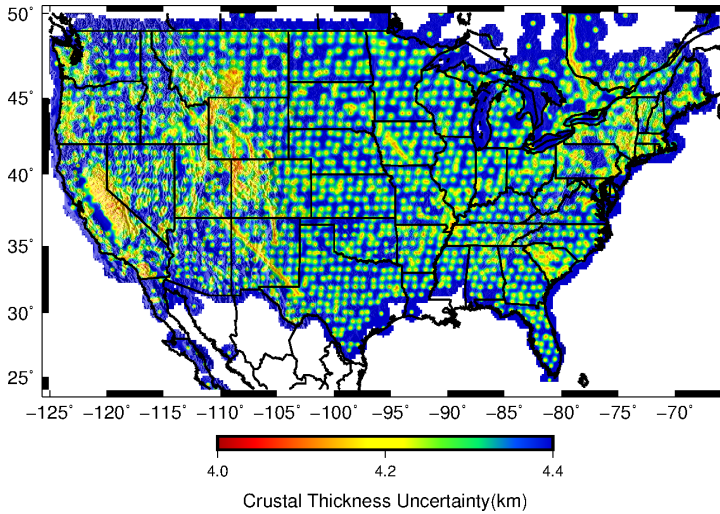
Figure 9. **One-sigma uncertainty of crustal thickness.** Uncertainty is estimated from optimal interpolation and hence strongly reflects the variogram statistics (Figure 5) used for interpolation, resulting in uncertainties ~4 km near seismic sites rising to above 4.8 km at distances beyond 70 km from the nearest station.

3.1 Model Uncertainty

Uncertainties of the crustal thickness and v_P/v_S estimates are given in Figures 9 and 10, respectively. Uncertainties are derived from the optimal interpolation procedure, which in turn uses the variogram spatial statistics (Figure 5) of the measurements at individual seismic sites to estimate both the interpolation weights for the expected value of a field and the estimate uncertainty. The error estimates are not comprehensive in that they neglect potential bias error that may arise from, e.g., an incorrect assumption of crustal v_P in generating our synthetic receiver functions. Optimal interpolation variance is given by the sum of the interpolation weights multiplied by the variogram variance expected for the distance between the interpolation point and the site associated with that weight, plus a slack variable that results from requiring interpolation weights to sum to one [e.g., *Davis*, 1986]. The weights are naturally largest for the nearest sites, so uncertainties in Figures 9 and 10 approximately reflect the variogram estimate (Figure 5) at the distance corresponding to the nearest seismic site.

3.2 Gravity Models

Estimation of the bulk crustal density and thickness contributions to observed Bouguer gravity is another significant result of this analysis. Figure 11 shows the gravity models associated with crustal thickness and v_P/v_S, calculated using the final inverted density parameters of $\Delta\rho_{\mathrm{Moho}}$ = 244 kg/m^3 and $\partial\rho/\partial(v_P/v_S)$ = 1212 kg/m^3. The density parameter estimates are much larger than those found by Lowry and Pérez-Gussinyé [2011], which were 115 and 460 kg/m^3 respectively. Density parameters found here are much closer to values expected based on laboratory and geophysical investigations because of the stochastic inversion approach used in this analysis (section 2.4). The Moho density contrast is nevertheless lower than, e.g., the 410 kg/m^3 reference value assumed for North America in Mooney and Kaban [2010]. Interestingly, the variance of the gravity associated with crustal composition implicit in v_P/v_S is slightly larger than that associated with crustal thickness: the root-mean square (RMS) of the gravity models are 58.9 mGal from crustal thickness variation and 60.0 mGal from v_P/v_S. This suggests that compositional density variations are a very significant (if not the largest) fraction of the total mass balance, and that it must

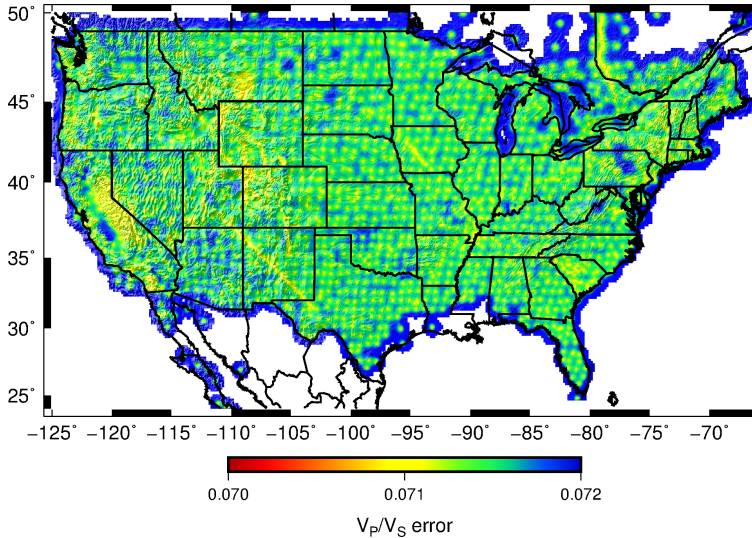be correctly accounted for in studies of elevation and lithospheric stress [e.g., *Becker et al.*, 2014].

Figure 10. One-sigma uncertainty of v_P/v_S. Uncertainty is estimated from optimal interpolation and hence strongly reflects the variogram statistics (Figure 5) used for interpolation, resulting in uncertainties ~0.070 near seismic sites rising to above 0.073 at distances beyond 70 km from the nearest station.

The residual Bouguer gravity after subtraction of contributions from crustal thickness, bulk compositional density and thermal variations is shown in Figure 12. The residual is greatly reduced, with RMS 56 mGal, relative to the 78 mGal RMS of the observed Bouguer gravity and a 112 mGal residual associated with the starting model derived from receiver function cross-correlation stacking. The residual gravity anomalies are likely dominated by asthenospheric mantle mass variations that our model does not account for [e.g., *Becker et al.*, 2014; 2015] and sphericity of the Earth, which produces anomalies that differ by up to tens of mGal from the Cartesian calculations used here on the scale of the conterminous U.S. The largest residuals appear to be dominated by a systematic pattern of greater asthenospheric mantle buoyancy in the west, resulting in residual anomalies mostly in the range of −150 to 50 mGal in the western U.S., but in the range −50 to 200 mGal in the east. Schmandt et al. [2015] inferred a ~200 kg/m^3 higher $\Delta\rho_{\mathrm{Moho}}$ west of −105°E longitude than in the eastern U.S., based on differences in the slope of crustal thickness versus elevation. We examined this hypothesis by separately inverting for the density contrast for the two halves, and found that gravity is best-fit with a Moho density contrast that is 63 kg/m^3 smaller in the east than in the west (Figure 13). There are other components of our model that might account for our east-west difference not being as large as that in Schmandt et al. [2015]: For example, our crustal v_P/v_S is noticeably lower on average in the west than in the east (Figure 8). If a roughly 0.08 mean difference in v_P/v_S were added to the Moho density contrast, it would increase the difference in eastern and western $\Delta\rho_{\mathrm{Moho}}$ by ~100 kg/m^3. On the other hand, the western U.S. mantle at 60 km depth averages 103°C hotter than in the east in our thermal model, which would translate to a 12 kg/m^3 reduction in the difference in eastern and western $\Delta\rho_{\mathrm{Moho}}$.

Gravity from Crustal Thickness (mgal)

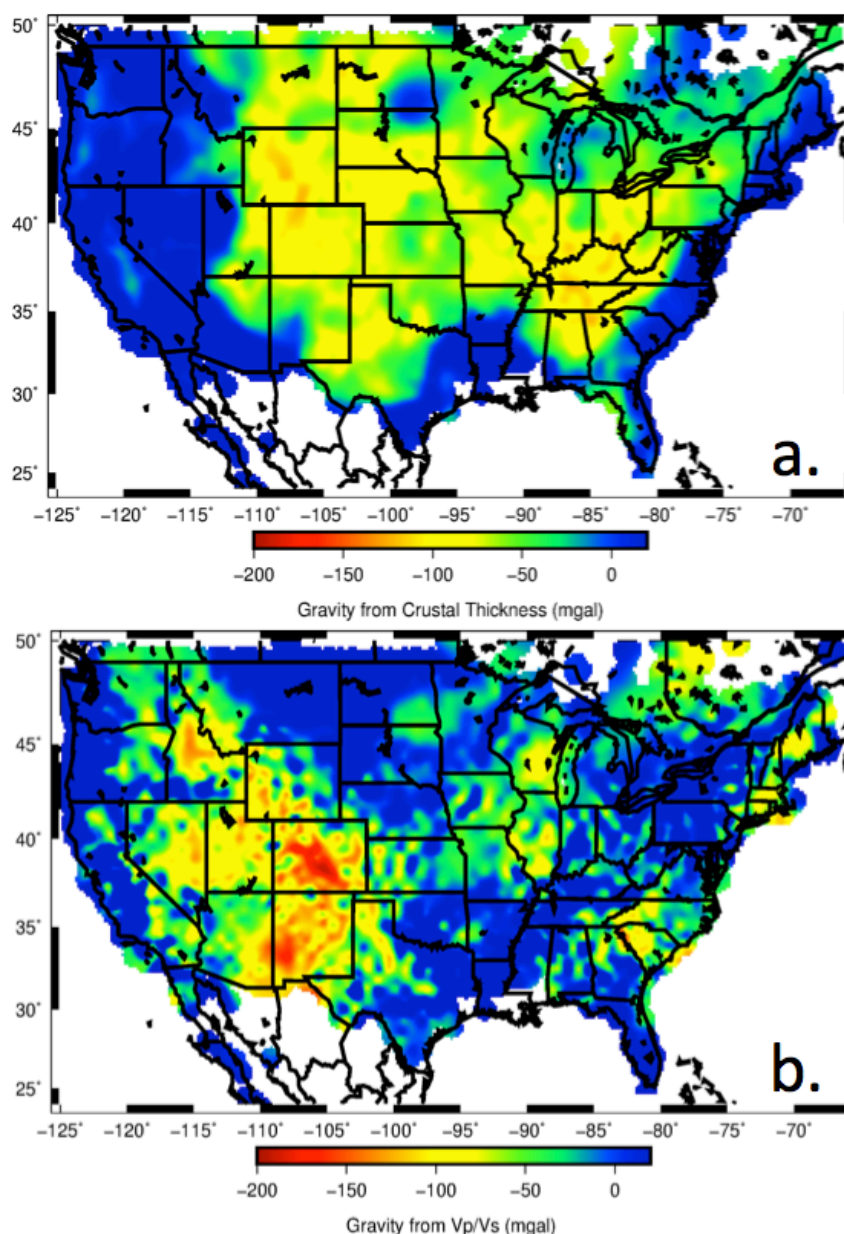

Gravity from Vp/Vs (mgal)

Figure 11. Modeled Bouguer gravity anomaly associated with (a) crustal thickness and (b) v_P/v_S. Gravity maps have been shifted by a datum corresponding to the difference between observed gravity and the (zero-mean) models.

Residual anomalies also may be amplified by melts present in the crust. For example, the High Lava Plains and northwestern Basin and Range exhibits high v_P/v_S (>1.9) associated with low observed Bouguer gravity where shear wave velocities and electrical conductivity indicate a lower crustal melt fraction as high as 3% [*Wagner et al.*, 2012; *Meqbel et al.*, 2014]. Partial melt raises the v_P/v_S with no corresponding increase in crustal density, resulting in a density derivative with opposite sign to the compositional trend that dominates our estimate of the density derivative. Consequently, the assumed constant density derivative overestimates the crustal compositional gravity anomaly where melt increases v_P/v_S.
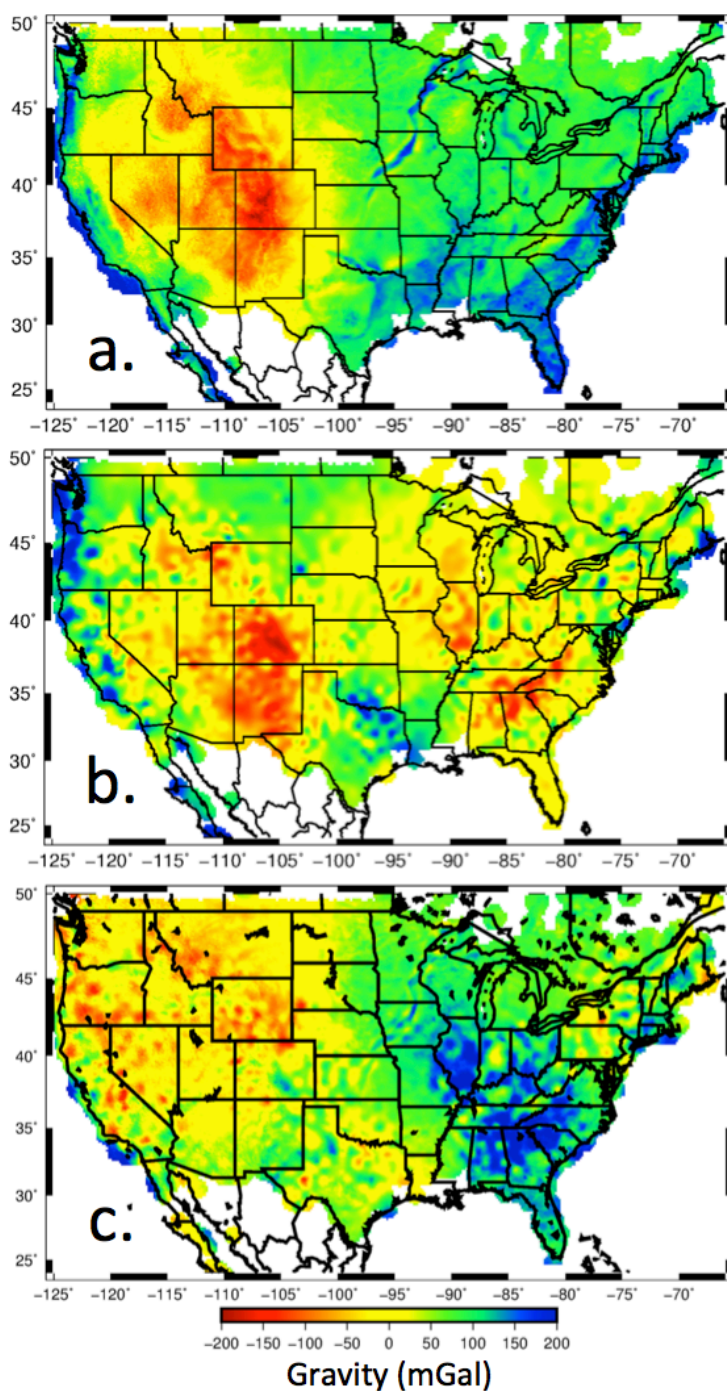
Figure 12. Bouguer gravity. (a) WGM2012 Bouguer gravity anomalies. (b) Modeled gravity anomalies summing the contributions from crustal thickness, crustal composition implicit in v_P/v_S, and thermal variations. (c) Residual after subtracting summed model contributions in (b) from measured gravity in (a).

4. Mineral Physics Modeling

The chemical composition and mineralogical makeup of continental crust has been examined for decades but remains a significant challenge [*Rudnick and Fountain*, 1995; *Rudnick and Gao*, 2003; *Hacker et al.*, 2015]. Sparse (and potentially biased) xenolith sampling of both localities and depth raises questions about how well the potential variability of deep continental crust is understood. Seismic imaging of the crust clearly has great potential for illuminating deep crustal variability, but is subject to its own limitations and ambiguities [*Christensen and Mooney*, 1995; *Christensen*, 1996]. However variations in the seismic velocity ratio v_P/v_S of crustal rocks, because of its insensitivity to temperature and comparatively high sensitivity to composition (and especially quartz content), shows some promise as an investigative tool for exploring crustal compositional variation [*Christensen*, 1996; *Lowry & Pérez-Gussinyé*, 2011].
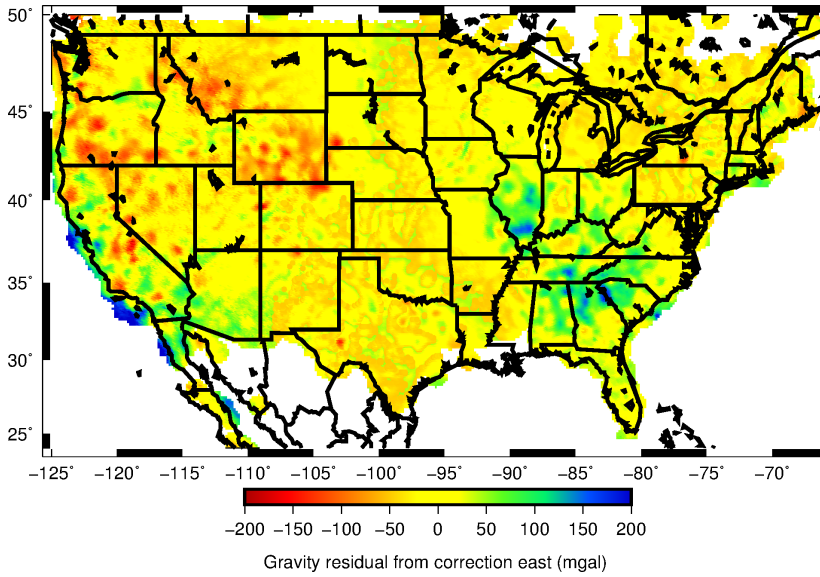
Figure 13. Residual Bouguer gravity after estimating the Moho density contrast separately for the eastern and western United States. Western U.S. gravity anomalies are similar to Figure 12, dominated by negative anomalies in the northern and middle Rocky Mountains and northern Basin and Range. However previously large positive anomalies in the eastern U.S. are greatly reduced, with most less than 100 mGal.

To more fully understand the possible implications of v_P/v_S and associated density variations for deep crustal composition and mineralogy, we used the thermodynamic model Perple_X [*Connolly*, 2009]. Perple_X's thermodynamical modeling of (pressure-, temperature, and chemistry-dependent) mineral equations of state calculates the likely assemblage of minerals using a linear programming minimization of the Gibbs free energy at given entropy and volume. Our modeling assumes crustal chemistries with weight percentage of components as described in Table 1, assuming three different major element chemistries corresponding to averages for the upper, middle and lower crust, based on Rudnick and Gao [2003]. The thermodynamical database is identical to that of Holland and Powell [1998]. The mineral solution [*Dale et al.*, 2000; *Holland and Powell*, 1996; 1998; 2001; 2003; *White et al.*, 2001] is included in Table S1 of the Supplementary Materials file.

Table 1: Average chemistry of upper, middle and lower continental crust from Rudnick and Gao [2003], used in modeling for this paper.

Wt-%	Na_2O	MgO	Al_2O_3	SiO_2	K_2O	FeO	CaO
upper crust	3.27	2.48	15.4	66.62	2.8	3.59	5.04
middle crust	3.39	3.59	15.00	63.5	2.3	5.25	6.02
lower crust	2.65	7.24	16.9	53.4	0.61	9.59	8.57

Guerri et al. [2015] earlier used Perple_X to examine how hydration state of crustal chemistries influenced geophysical properties of seismic velocity and density. Although the seismic velocity ratio was not a primary target for their analyses, they did note in passing that hydration reduces v_P/v_S. Our modeling is undertaken here to

replicate their result, to examine why v_P/v_S decreases (e.g., address how much is related to increased abundance of quartz versus changes to velocity properties of other minerals), and to more fully understand how hydration affects other physical properties of the crust including temperature.
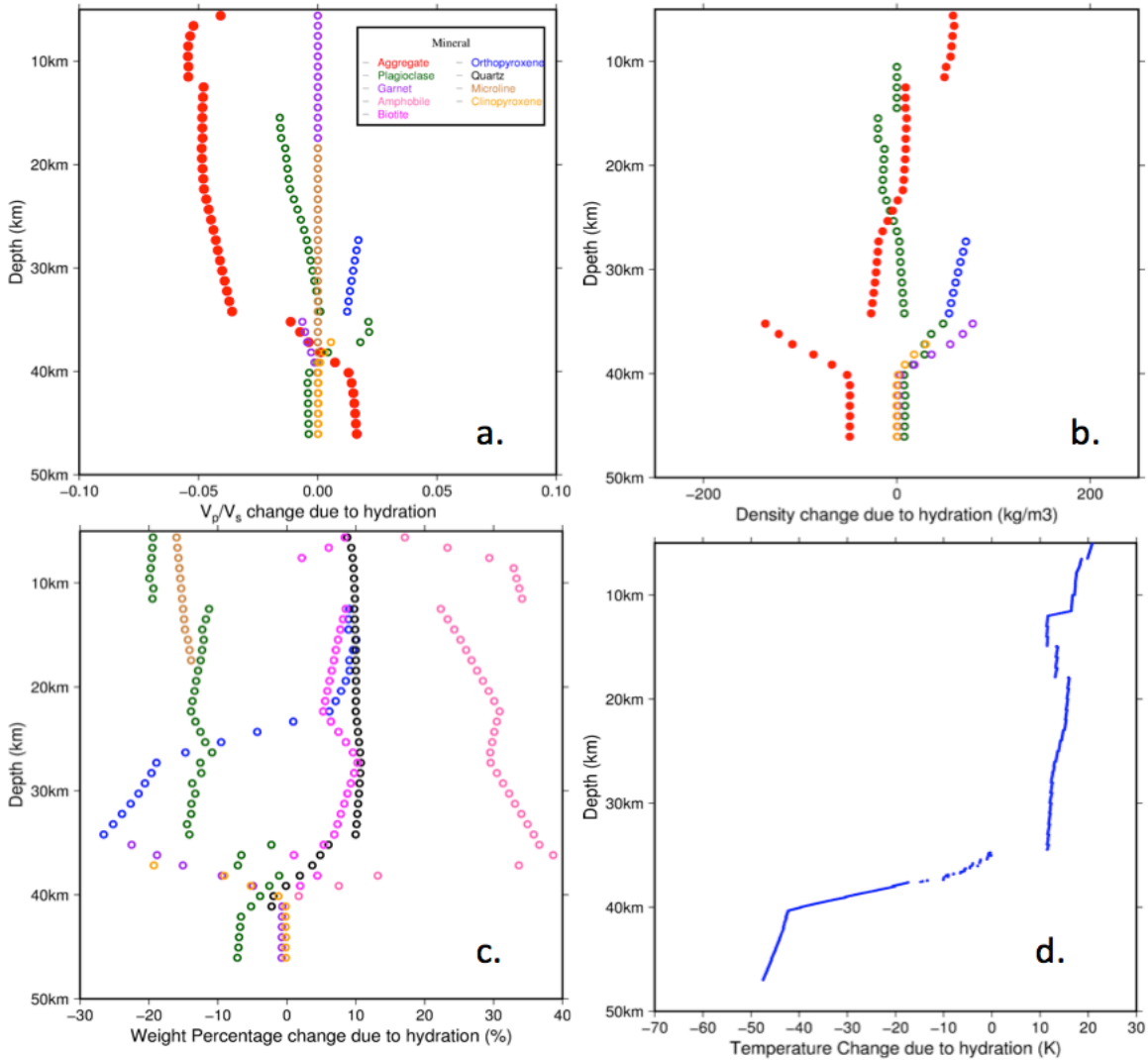

Figure 14. Difference in mineralogy and geophysical properties from Perple_X modeling [*Connolly*, 2009] of a mid-crustal chemistry with and without 1 wt-% water (hydrated minus dry). (a) Hydration produces no change in v_P/v_S of most minerals excepting a small decrease in v_P/v_S of plagioclase, but the aggregate change in v_P/v_S is large. (b) Changes in density of individual minerals are also small relative to the aggregate change. (c) The wt-% of mineral constituents changes significantly, indicating aggregate changes in v_P/v_S reflect increased quartz and density is dominated by consumption of garnet and pyroxene (refer to Figure 1 for properties of these minerals). (d) Temperature change from change of mineral enthalpy, assuming no change in original entropy.

All of our thermodynamical models sampled the crust at 1 km depth intervals using the weight of the crustal column for pressure and geotherms derived from our thermal model (section 2.7). In some models, we interpolated smoothly over depth a

changing chemistry based on the layer average chemistries in Table 1; for others we used a constant mid-crustal chemistry in order to more easily distinguish effects of phase boundaries from those of changing chemistry. Figure 14 shows one example of our modeling in which we used a midcrustal chemistry (i.e., no change with depth) and modeled the changes that result with and without a 1 wt-% water constituent included. The thermodynamical modeling predicts the v_P/v_S ratio of a dry chemistry increases gradually with depth from 1.72–1.75 (Figure 14a), as the wt-% of quartz gradually decreases. Adding a 1 wt-% water constituent significantly reduces plagioclase, orthopyroxene and microcline in the aggregate while increasing the quartz constituent by up to 10 wt-%, resulting in a significant reduction of v_P/v_S at all depths except where melt is produced (in this example, below 40 km, but the geotherm used was from the Basin and Range province where the crust is not that thick). The density is also reduced, but the greatest reduction of density occurs deep in the crustal column where garnet is consumed by hydration (consistent with the interpretation of xenoliths from the U.S. Cordillera by Jones et al. [2015]).

The model in Figure 14a predicts a bulk-crustal v_P/v_S near 1.75 for a dry crustal column and 1.65 for hydrated. The average v_P/v_S ratio from our joint inversion is 1.79, which is more consistent with typical values for crustal rocks from lab experiments [*Christensen*, 1996]. The lower model v_P/v_S might reflect some error in the equations of state relating to the Poisson's ratio. It is also possible that the chemistry profile from Rudnick and Gao [2003] adopted in the modeling depicted in Figure 14 is not representative of the mean chemistry of North American crust, or that the equations of state specified in the Perple_X modeling are slightly in error. Nevertheless, the primary conclusion we draw from the modeling is liable to be true regardless: Hydration increases the abundance of quartz, consumes pyroxenes, feldspars and garnets, and consequently reduces bulk v_P/v_S and density of the crustal column. Hence, low bulk crustal v_P/v_S in Figure 8 can be considered indicative of a hydration event at some point during the evolution of the crust.

Another interesting implication of the Perple_X modeling in Figure 14 is that hydration results in a complicated thermal profile for the crust. Above the ~35 km depth where orthopyroxene and plagioclase break down to form clinopyroxene and garnet, hydration reactions are exothermic and would be expected to raise crustal temperatures by 10–20°C. Below that phase boundary however, hydration reactions are endothermic and would be expected to reduce temperatures by as much as 50°C for 1 wt-% water, largely because of the latent heat of fusion required for melting of garnet that results from the hydration. Hence, hydration of the entire crustal column would be expected to increase surface heat flow by increasing advective heat transfer associated with melt and volatile flux, raising temperatures in the shallow crust via reaction thermodynamics, and simultaneously lowering temperatures in the lower crust and at the Moho where heat is consumed by melt. A large discrepancy between surface heat flow and Pn-derived Moho temperatures has been observed under high elevations of the western U.S. Cordillera [*Berry et al.*, 2015], with colder-than-expected Moho prevalent in regions of the Basin and Range and Rocky Mountains where we observe very low v_P/v_S.

5. Discussion

Much of what we know about the compositional variation of continental crust is derived from observations of surface exposures of crystalline basement and sparse xenoliths brought to the surface by volcanism [*Rudnick and Fountain*, 1995; *Hacker et al.*, 2015; *Weber et al.*, 2002], and these types of studies suggest that regional differences in bulk chemistry are small (of order 1%). Many studies have also examined relationships between mineral composition and seismic velocities [e.g., *Miller and Christensen*, 1994; *Sobolev and Bakeyko*, 1994; *Christensen and Mooney*, 1995; *Kern et al.*, 1996; *Musacchio et al.*, 1997; *Hacker et al.*, 2015], but the temperature and melt-dependence of velocities, plus the wide range of compositions consistent with a given velocity, make interpretation ambiguous.

The seismic velocity ratio, v_P/v_S, also is non-unique with respect to composition and melt, but its relative insensitivity to temperature and high sensitivity to quartz content makes it a potentially valuable tool for investigation of crustal compositional variation [*Christensen and Fountain*, 1975; *Kern*, 1982; *Holbrook et al.*, 1992; *Zandt et al.*, 1994; *Christensen*, 1996; *Lowry and Pérez-Gussinyé*, 2011]. Guerri et al. [2015] noted that hydration lowers Poisson's ratio (and hence v_P/v_S) based on their results of Perple_X modeling of mineral thermodynamics similar to that performed here. The thermodynamical modeling of mineralogy described here further clarifies that hydration increases the abundance of quartz at the expense of pyroxene, feldspar and mica. This is also consistent with an observed systematic relationship observed between v_P/v_S and depth to the subduction plate interface in Cascadia [*Audet and Bürgmann*, 2014], which had been interpreted as evidence of progressive quartz precipitation and mineralization in veins but more likely reflects hydration state of the overlying crust. Hence, greater quartz abundance evidenced by lower crustal v_P/v_S may prove a reliable indicator of hydration history of the crust.

Viewed from that perspective, Figure 8 can be considered as at least partly reflecting the hydration state of the crust. This has implications that may extend far beyond just processes of volatile transfer through the crust. For example, hydration state is one of the primary factors determining rheological strength of rocks in the ductile flow regime [e.g., *Mackwell et al.*, 1985; *Bürgmann and Dresen*, 2008]. Hydration also affects density (Figure 14b), most significantly by consuming garnet in lower crustal P-T conditions.

Jones et al. [2015] cited hydration observed in a handful of lower crustal xenoliths as evidence that hydration and resulting expansion of the lower crust may be responsible for a significant fraction of elevation of the western United States Cordillera following the Laramide flat slab episode. This interpretation is supported by the imaging results and modeling described in this paper. Moreover, it raises some interesting possible implications for the nature of Laramide-style, thick-skin contractional tectonics. The curious nature of such tectonism, characterized by high-angle thrust faulting at odd and highly variable angles to any presumptive regional plate-tectonic stress geometry, makes some sense if we recognize that these structures are found almost exclusively in the vicinity of flat-slab style subduction

and may actually reflect a response to simultaneous weakening and volumetric expansion of lower crustal mineral assemblages by hydration. Such a hypothesis raises other questions however, including what volumes of hydrous mass transport are needed to achieve widespread hydration of a significant fraction of the crust in these regions, and how such widespread volatile transport would affect thermal transport through the crust.

The thermodynamical modeling indicates that temperatures are reduced by hydration in the lower crust but increased in the upper crust (Figure 14d). This is especially intriguing in light of observations that, in regions of high Cordilleran elevation, Moho temperatures derived from Pn velocities are much lower than one would anticipate based on conductive thermal modeling of surface heat flow measurements [*Berry et al*., 2015]. If hydration reaction thermodynamics turns out to be an observable phenomenon, this would provide a potentially useful constraint on the timing of hydration. Much of the low v_P/v_S observed in Figure 8 is found in regions where hydration undoubtedly occurred long ago (e.g., in the Appalachian Piedmont to Valley and Ridge; Interior Plains central lowlands and adjacent to the Midcontinent rift). The timescale for conductive thermal transport through the lithosphere is roughly 100 million years, so observing a thermal signature associated with hydration reactions would imply that the hydration event is more recent than that.

6. Conclusions

Receiver function estimates of thickness and seismic velocity ratios, v_P/v_S, of U.S. continental crust within the EarthScope footprint are greatly improved by joint inversion with likelihood filters derived from gravity modeling and spatial statistics. Crustal thickness averaged over the conterminous U.S. is 38.9 km, and averaged v_P/v_S is 1.79.

Crustal thickness (Figure 7) exhibits many interesting relationships to physiographic and basement provinces, even in the central and eastern U.S. where these are not forced by active tectonism. Crust is thickest in the southern Rocky Mountains and Appalachian Highlands, consistent with earlier inferences from seismic refraction surveys [*Braile et al*., 1989; *Taylor*, 1989] as well as with other tomographic and receiver function models derived from EarthScope data [*Shen et al*., 2016; *Schmandt et al*., 2015].

As measured by modeled contributions to the variance of gravity, the largest contributor to mass variation in the U.S. lithosphere is compositional variation within the crust, followed by variations in crustal thickness and finally geothermal variations. After subtracting gravity anomalies due to crustal composition, thickness and thermal variation from measured Bouguer gravity, most of the residual gravity is likely related to asthenospheric mantle density variations [e.g., *Becker et al*., 2014], although some residual gravity anomalies may be amplified by the presence of crustal melts. The gravity residual is reduced if we allow for differences in reference Moho density contrast in the eastern (172 kg/m^3) and western (235 kg/m^3) United States, similar to that previously proposed by Schmandt et al. [2015].

Modeling of the thermodynamics of mineral formation suggests that hydration of crustal mineral assemblages significantly impacts several geophysical properties that may be observable by geophysical remote sensing methods. Hydration increases the abundance of quartz (Figure 14c), which reduces the seismic velocity ratio in the middle and upper crust (Figures 1 and 14a). Hydration also reduces density in the lower crust by consuming garnet (Figure 14b), and consequently water derived from dehydration of the Farallon slab during its Laramide phase of flattened geometry [*Humphreys et al.*, 2003] may be partly responsible for post-Laramide elevation of the Intermountain western U.S. [e.g., *Jones et al.*, 2015]. Finally, hydration reactions are exothermic in the upper crust, which would express as enhanced surface heat flow coincident with low crustal v_P/v_S (as observed by Lowry and Pérez-Gussinyé [2011]). However, hydration is endothermic in the lower crust where garnets are consumed to form melts, which should cool the Moho and may result in large discrepancies between Pn-derived estimates of Moho temperature and predictions of deep temperature derived from surface heat flow in regions of high elevation [*Berry et al.*, 2015].

ACKNOWLEDGMENTS

4. References

Afonso, J. C., G. Ranalli, and M. Fernandez (2005), Thermal expansivity and elastic properties of the lithospheric mantle: results from mineral physics of composites, *Phys. Earth Planet. Int.*, 149(3), 279-306, doi:10.1016/j.pepi.2004.10.003.

Afonso, J. C., N. Rawlinson, Y. Yang, D. L. Schutt, A. G. Jones, J. Fullea, and W. L. Griffin (2016), 3D multi-observable probabilistic inversion for the compositional and thermal structure of the lithosphere and upper mantle: III. Thermochemical tomography in the Western–Central US, *J. Geophys. Res.*, 121(10), 7337-7370.

Ammon, C. J. (1991), The isolation of receiver effects from teleseismic P waveforms, *Bull. Seismol. Soc. Am.*, 81(6), 2504-2510.

Audet, P., and R. Bürgmann (2014), Possible control of subduction zone slow-earthquake periodicity by silica enrichment, *Nature*, 510(7505), 389-392, doi:10.1038/nature13391.

Balmino, G., N. Vales, S. Bonvalot, and A. Briais (2011), Spherical harmonic modeling to ultra-high degree of Bouguer and isostatic anomalies, *J. Geod.*, 86(7), 499-520, doi: 10.1007/s00190-011-0533-4.

Beck, J. V. and K. J. Arnold (1977), *Parameter Estimation in Engineering and Science*, John Wiley & Sons, New York.

Becker, T. W., C. Faccenna, E. D. Humphreys, A. R. Lowry, and M. S. Miller (2014), Static and dynamic support of western United States topography, *Earth Planet. Sci. Lett.*, 402, 234-246, doi:10.1016/j.epsl.2013.10.012.

Becker, T. W., A. R. Lowry, C. Faccenna, B. Schmandt, A. Borsa, and C. Yu (2015), Western US intermountain seismicity caused by changes in upper mantle flow, *Nature*, 524(7566), 458-461, doi:10.1038/nature14867.

Berry, M. A., A. R. Lowry, D. L. Schutt, and R. V. S. Kanda (2014), Crustal geothermal properties and evidence of Laramide thermal perturbation of the western United States, Abstr. #T22B-04, AGU Fall Mtg, San Francisco CA.

Berry, M. A., A. R. Lowry, D. L. Schutt, R. V. S. Kanda, and J. S. Buehler (2015), Cold and wet at the roots of U.S. Cordilleran high elevation, Abstr. #T11C-2910, AGU Fall Mtg, San Francisco CA.

Bonvalot, S., G. Balmino, A. Briais, M. Kuhn, A. Peyrefitte, N. Vales, R. Biancale, G. Gabalda, F. Reinquin, and M. Sarrailh (2012), World Gravity Map, *Bureau Gravimetrique International* (*BGI*), Map, CGMW-BGI-CNES728, IRD, Paris.

Braile, L. W., W. J. Hinze, R. R. B. Von Frese, and G. R. Keller (1989), Seismic properties of the crust and uppermost mantle of the conterminous United States and adjacent Canada. *Geol. Soc. Am. Mem.*, 172, 655-680, doi:10.1130/MEM172-p655.

Buehler, J. S., and P. M. Shearer (2014), Anisotropy and V_p/V_s in the uppermost mantle beneath the western United States from joint analysis of Pn and Sn phases, *J. Geophys. Res.*, 119(2), 1200-1219, doi:10.1002/2013JB010559.

Buehler, J. S., and P. M. Shearer (2017), Uppermost mantle seismic velocity structure beneath USArray, *J. Geophys. Res.*, in press, doi:10.1002/2016JB013265.

Bürgmann, R., and G. Dresen (2008), Rheology of the lower crust and upper mantle: Evidence from rock mechanics, geodesy, and field observations, *Annu. Rev. Earth Planet. Sci.*, 36, 531-567, doi: 10.1146/annurev.earth.36.031207.124326.

Christensen, N. I. (1996), Poisson's ratio and crustal seismology, *J. Geophys. Res.*, 101(B2), 3139-3156, doi:10.1029/95JB03446.

Christensen, N. I., and D. M. Fountain (1975), Constitution of the lower continental crust based on experimental studies of seismic velocities in granulite, *Geol. Soc. Am. Bull.*, 86(2), 227-236, doi:10.1130/0016-7606(1975)86<227:COTLCC>2.0.CO;2.

Christensen, N., and W. Mooney (1995), Seismic velocity structure and composition of the continental crust: A global view, *J. Geophys. Res.*, 100(B6), 9761-9788, doi:10.1029/95JB00259.

Connolly, J. A. D. (2009) The geodynamic equation of state: what and how, *Geochem. Geophys. Geosys.*, 10(10), doi:10.1029/2009GC002540.

Crotwell, H. P., and T. J. Owens (2005), Automated receiver function processing, *Seismol. Res. Lett.*, 76(6), 702-709, doi:10.1785/gssrl.76.6.702.

Dale, J., Holland, T. and Powell, R. (2000), Hornblende–garnet–plagioclase thermobarometry: a natural assemblage calibration of the thermodynamics of hornblende, *Contrib. Min. Pet.*, 140(3), 353-362, doi: 10.1007/s004100000187.

Davis, J. C. (1986), *Statistics and Data Analysis in Geology* (2nd edn), Wiley, New York.

DePaolo, D. J., T. E. Cerling, S. R. Hemming, A. H. Knoll, F. M. Richter, L. H. Royden, R. L. Rudnick, L. Stixrude, and J. S. Trefil (2008), *Origin and evolution of Earth: Research questions for a changing planet*, National Academies Press, Washington D.C.

Dziewonski, A. M., and D. L. Anderson (1981), Preliminary reference Earth model, *Phys. Earth Planet. Int.*, 25(4), 297-356, doi:10.1016/0031-9201(81)90046-7.

Ehlers, T. A. (2005), Crustal thermal processes and the interpretation of thermochronometer data, *Rev. Mineral. Geochem.*, 58(1), 315-350, doi:10.2138/rmg.2005.58.12.

Guerri, M., F. Cammarano, and J. A. Connolly (2015), Effects of chemical composition, water and temperature on physical properties of continental crust, *Geochem. Geophys. Geosys.*, 16(7), 2431-2449, doi:10.1002/2015GC005819.

Hacker, B. R., P. B. Kelemen, and M. D. Behn (2015), Continental lower crust, *Ann. Rev. Earth Planet. Sci.*, 43, 167-205, doi:10.1146/annurev-earth-050212-124117.

Holbrook, W. S., W. D. Mooney, and N. I. Christensen (1992), The seismic velocity structure of the deep continental crust, in *Continental Lower Crust*, edited by D. M. Fountain, R. Arculus, and R. W. Kay, pp. 1–43, Elsevier Sci., New York.

Holland, T. and Powell, R. (1996), Thermodynamics of order-disorder in minerals: II. Symmetric formalism applied to solid solutions, *Am. Mineral.*, 81(11-12), 1425-1437, doi:10.2138/am-1996-11-1215.

Holland, T. J. B., and Powell, R. (1998), An internally consistent thermodynamic data set for phases of petrological interest, *J. Metamorph. Geol.*, 16(3), 309-343.

Holland, T. I. M. and Powell, R. (2001), Calculation of phase relations involving haplogranitic melts using an internally consistent thermodynamic dataset, *J. Petrol.*, 42(4), 673-683, doi:10.1093/petrology/42.4.673.

Holland, T. and Powell, R. (2003), Activity–composition relations for phases in petrological calculations: an asymmetric multicomponent formulation, *Contrib. Mineral. Petrol.*, 145(4), 492-501, doi:10.1007/s00410-003-0464-z.

Humphreys, E., E. Hessler, K. Dueker, G. L. Farmer, E. Erslev, and T. Atwater (2003), How Laramide-age hydration of North American lithosphere by the Farallon slab controlled subsequent activity in the western United States, *Int. Geol. Rev.*, 45(7), 575-595, doi: 10.2747/0020-6814.45.7.575.

IRIS DMC (2010), Data Services Products: EARS EarthScope Automated Receiver Survey, doi:10.17611/DP/EARS.1.

Ito, T., and M. Simons (2011), Probing asthenospheric density, temperature, and elastic moduli below the western United States, *Science*, 332(6032), 947-951.

Jones, C. H., K. H. Mahan, L. A. Butcher, W. B. Levandowski, and G. L. Farmer (2015), Continental uplift through crustal hydration, *Geology*, 43(4), 355-358, doi:10.1130/ G36509.1.

Julià, J. (2007), Constraining velocity and density contrasts across the crust—mantle boundary with receiver function amplitudes, *Geophys. J. Int.*, 171(1), 286-301, doi: 10.1111/j.1365-2966.2007.03502.x.

Kern, H. (1982), Elastic-wave velocity in crustal and mantle rocks at high pressure and temperature: The role of the high-low quartz transition and of dehydration reactions, *Phys. Earth Planet. Int.*, 29(1), 12-23, doi:10.1016/0031-9201(82)90133-9.

Kern, H., S. Gao, and Q. S. Liu (1996), Seismic properties and densities of middle and lower crustal rocks exposed along the North China Geoscience Transect, *Earth Planet. Sci. Lett.*, *139*(3-4), 439-455, doi:10.1016/0012-821X(95)00240-D.

Kohlstedt, D. L. (2006), The role of water in high-temperature rock deformation, *Rev. Mineral. Geochem.*, 62(1), 377-396, doi:10.2138/rmg.2006.62.16.

Kono, Y., A. Miyake, M. Ishikawa, and M. Arima (2008), Temperature derivatives of elastic wave velocities in plagioclase (An51±1) above and below the order-disorder transition temperature, *Am. Mineralog.*, 93(4), 558-564, doi:10.2138/am.2008.2591.

Levander, A., and M. S. Miller (2012), Evolutionary aspects of lithosphere discontinuity structure in the western US, *Geochem. Geophys. Geosys.*, 13(7), doi:10.1029/ 2012GC004056.

Ligorría, J. P., and C. J. Ammon (1999), Iterative deconvolution and receiver-function estimation, *Bull. Seismol. Soc. Am.*, 89(5), 1395-1400.

Lin, F. C., B. Schmandt, and V. C. Tsai (2012), Joint inversion of Rayleigh wave phase velocity and ellipticity using USArray: Constraining velocity and density structure in the upper crust, *Geophys. Res. Lett.*, 39(12), doi:10.1029/2012GL052196.

Lowry, A. R., and M. Pérez-Gussinyé (2011), The role of crustal quartz in controlling Cordilleran deformation, *Nature*, 471(7338), 353-357, doi:10.1038/nature09912.

Lowry, A. R., N. M. Ribe, and R. B. Smith (2000), Dynamic elevation of the Cordillera, western United States, *J. Geophys. Res.*, 105(B10), 23371-23390, doi: 10.1029/2000JB900182.

Lyman, E. (2016), *Mineral Physics Modeling of the Effect of Water on Crustal Seismic Velocity Ratios*, undergraduate research thesis, Utah State University.

Mackwell, S. J., D. L. Kohlstedt, and M. S. Paterson (1985), The role of water in the deformation of olivine single crystals, *J. Geophys. Res.*, 90(B13), 11319-11333, doi: 10.1029/JB090iB13p11319.

Martinec, Z. (1994), The density contrast at the Mohorovičic discontinuity, *Geophys. J. Int.*, 117(2), 539-544, doi:10.1111/j.1365-246X.1994.tb03950.x.

McCurry, M., and D. W. Rodgers (2009), Mass transfer along the Yellowstone hotspot track I: Petrologic constraints on the volume of mantle-derived magma. *J. Volcanol. Geotherm. Res.*, 188(1), 86-98, doi:10.1016/j.jvolgeores.2009.04.001.

Meqbel, N. M., G. D. Egbert, P. E. Wannamaker, A. Kelbert, and A. Schultz (2014), Deep electrical resistivity structure of the northwestern US derived from 3-D inversion of USArray magnetotelluric data, Earth Planet. Sci. Lett., 402, 290-304, doi: 10.1016/j.epsl.2013.12.026.

Miller, D. J., and N. L. Christensen (1994), Seismic signature and geochemistry of an island arc: A multidisciplinary study of the Kohistan accreted terrane, northern Pakistan, *J. Geophys. Res.*, 99(B6), 11623-11642.

Mooney, W. D., and M. K. Kaban (2010), The North American upper mantle: Density, composition, and evolution, *J. Geophys. Res.*, 115(B12), doi:10.1029/2010JB000866.

Musacchio, G., W. D. Mooney, J. H. Luetgert, and N. I. Christensen (1997), Composition of the crust in the Grenville and Appalachian Provinces of North America inferred from V_p/V_s ratios, *J. Geophys. Res.*, 102(B7), 15225-15241, doi:10.1029/96JB03737.

Niu, F., and D. E. James (2002), Fine structure of the lowermost crust beneath the Kaapvaal craton and its implications for crustal formation and evolution, *Earth Planet. Sci. Lett.*, 200(1), 121-130, doi:10.1016/S0012-821X(02)00584-8.

Pakiser, L. C. (1989), Geophysics of the Intermontane system, *Geol. Soc. Am. Mem.*, *172*, 235-248, doi:10.1130/MEM172-p235.

Porter, R., Y. Liu, and W. E. Holt (2016), Lithospheric records of orogeny within the continental U.S., *Geophys. Res. Lett.*, 43(1), 144-153., doi:10.1002/2016JB012887.

Prodehl, C. (1970) Seismic refraction study of crustal structure in the western United States. *Geol. Soc. Am. Bull.*, 81(9), 2629-2646, doi:10.1130/0016-7606(1970)81[2629: SRSOCS]2.0.CO;2.

Rudnick, R. L., and D. M. Fountain (1995), Nature and composition of the continental crust: a lower crustal perspective, *Rev. Geophys.*, 33(3), 267-309, doi:10.1029/95RG01302.

Rudnick, R. L., and S. Gao (2003), The composition of the continental crust, in *The Crust*, edited by R. L. Rudnick, pp. 1–64, Elsevier-Pergamon, Oxford, U. K., doi:10.1016/B0-08-043751-6/03016-4

Schmandt, B., and E. Humphreys (2011), Seismically imaged relict slab from the 55 Ma Siletzia accretion to the northwest United States, *Geology*, 39(2), 175-178, doi: 10.1130/G31558.1.

Schmandt, B., F. C. Lin, and K. E. Karlstrom (2015), Distinct crustal isostasy trends east and west of the Rocky Mountain Front, *Geophys. Res. Lett.*, 42(23), 10290-10298, doi:10.1002/2015GL066593.

Schulte-Pelkum, V., and K. H. Mahan (2014), A method for mapping crustal deformation and anisotropy with receiver functions and first results from USArray, *Earth Planet. Sci. Lett.*, 402, 221-233, doi:10.1016/j.epsl.2014.01.050.

Schutt, D. L., A. R. Lowry, and J. S. Buehler (2016), Moho temperature and compositional controls on lithospheric bending strength in the western United States, Abstr. #T23E-03, AGU Fall Mtg, San Francisco CA.

Schutt, D. L., A. R. Lowry, and J. S. Buehler (2017), Moho temperature and mobile lower crust in the western United States, submitted to *Geology*.

Shen, W., and M. H. Ritzwoller (2016), Crustal and uppermost mantle structure beneath the United States, *J. Geophys. Res.*, 121(6), 4306-4342, doi:10.1002/2016JB012887.

Smith, L., and D. S. Chapman (1983), On the thermal effects of groundwater flow: 1. Regional scale systems, *J. Geophys. Res.*, 88(B1), 593-608, doi:10.1029/JB088iB01p00593.

Smith, R. B., W. C. Nagy, K. A. S. Julander, J. J. Viveiros, C. A. Barker, and D. G. Gants (1989), Geophysical and tectonic framework of the eastern Basin and Range-Colorado Plateau-Rocky Mountain transition, *Geol. Soc. Am. Mem.*, *172*, 205-234, doi:10.1130/MEM172-p205.

Sobolev, S. V., and A. Y. Babeyko (1994), Modeling of mineralogical composition, density and elastic wave velocities in anhydrous magmatic rocks, *Surv. Geophys.*, *15*(5), 515-544, doi:10.1007/BF00690173.

Solano, J. M. S., M. D. Jackson, R. S. J. Sparks, J. D. Blundy, and C. Annen (2012), Melt segregation in deep crustal hot zones: a mechanism for chemical differentiation, crustal assimilation and the formation of evolved magmas, *J. Petrol.*, 53(10), 1999-2026, doi:10.1093/petrology/egs041.

Steck, L. K., M. L. Begnaud, S. Phillips, and R. Stead (2011), Tomography of crustal P and S travel times across the western United States, *J. Geophys. Res.*, 116(B11), doi:10.1029/ 2011JB008260.

Taylor, S. R. (1989), Geophysical framework of the Appalachians and adjacent Grenville Province, *Geol. Soc. Am. Mem.*, 172, 317-348, doi:10.1130/MEM172-p317.

Tenzer, R., P. Novák, V. Gladkikh, and P. Vajda (2012), Global crust-mantle density contrast estimated from EGM2008, DTM2008, CRUST2.0, and ICE-5G, *Pure Appl. Geophys.*, 169(9), 1663-1678, doi:10.1007/s00024-011-0410-3.

Trabant, C., A. R. Hutko, M. Bahavar, R. Karstens, T. Ahern, and R. Aster (2012), Data Products at the IRIS DMC: Stepping Stones for Research and Other Applications, *Seismol. Res. Lett.*, 83(5), 846–854, doi:10.1785/0220120032.

Wagner, L. S., M. J. Fouch, D. E. James, and S. Hanson Hedgecock (2012), Crust and upper mantle structure beneath the Pacific Northwest from joint inversions of ambient noise and earthquake data, *Geochem. Geophys. Geosys.*, *13*(12), doi:10.1029/2012GC004353.

Weber, M. B., J. Tarney, P. D. Kempton, and R. W. Kent (2002), Crustal make-up of the northern Andes: evidence based on deep crustal xenolith suites, Mercaderes, SW Colombia, *Tectonophysics*, 345(1), 49-82, doi:10.1016/S0040-1951(01)00206-2.

White, R. W., Powell, R., and Holland, T. J. B. (2001), Calculation of partial melting equilibria in the system $Na_2O–CaO–K_2O–FeO–MgO–Al_2O_3–SiO_2–H_2O$ (NCKFMASH), *J. Metamorph. Geol.*, 19(2), 139-153, doi:10.1046/j.0263-4929.2000.00303.x.

Whitmeyer, S. J., and K. E. Karlstrom (2007), Tectonic model for the Proterozoic growth of North America, *Geosphere*, 3(4), 220-259, doi:10.1130/GES00055.1.

Williams, M.L., K.M. Fischer, J.T. Freymueller, B. Tikoff, A.M. Tréhu, et al., (2010), *Unlocking the Secrets of the North American Continent: An EarthScope Science Plan for 2010-2020*, 78 pp.

Zandt, G., S. C. Myers, and T. C. Wallace (1995), Crust and mantle structure across the Basin and Range Colorado Plateau boundary at 37 N latitude and implications for Cenozoic extensional mechanism, *J. Geophys. Res.*, 100(B6), 10529-10548, doi: 10.1029/94JB03063.

Zhu, L., and H. Kanamori (2000), Moho depth variation in southern California from teleseismic receiver functions, *J. Geophys. Res.*, 105(B2), 2969-2980, doi: 10.1029/1999JB900322.